



Fostering the clean transport transition for a healthy place to live!

## **Co-generation of hydrogen and electricity with high-temperature fuel cells**

### **D1.7: Report on stack lifetime prediction**

***WP1, T***

***30/06/2020***

Research & Innovation Action– GRANT AGREEMENT No. 735692



*This project has received funding from the Fuel Cells and Hydrogen 2 Joint Undertaking under grant agreement No 735692. This Joint Undertaking receives support from the European Union's Horizon 2020 research and innovation programme, Hydrogen Europe and Hydrogen Europe Research.*



## Technical References

Project Acronym	CH2P
Project Title	Co-generation of hydrogen and electricity with high-temperature fuel cells
Project Coordinator	Luigi Crema - FBK <a href="mailto:crema@fbk.eu">crema@fbk.eu</a>
Project Duration	February 1, 2017 - July 31, 2020 (42 Months)

Deliverable No.	D1.7
Dissemination Level	CO/PU
Work Package	WP1 – TECHNOLOGY SCENARIO AND DESIGN
Task	T 1.5 - STACK DURABILITY MODELLING
Lead beneficiary	4 -EPFL
Contributing beneficiary(ies)	2-(SP), 3-(HTc), 4 (EPFL)
Due date of deliverable	31 April 2020
Actual submission date	30 June 2020
Estimated person-month for deliverable	24

## Versions

Revision Version	Date	Changes	Changes made by Partner
0.1	30/03/2020	Table of Content	Hamza Moussaoui (EPFL)
1.0	29/04/2020	First draft	Hamza Moussaoui (EPFL), Fabio Greco (EPFL), Giorgio Rinaldi (EPFL), Arata Nakajo (EPFL)
2.0	29/05/2020	Revisions	Jan Van herle (EPFL), Hamza Moussaoui (EPFL)
2.1	30/06/2020	Quality check	Jeroen Brenkman (SHELL), Elli Varkaraki (SP), Chiara Pellegrini (FBK), Hamza Moussaoui (EPFL), Luigi Crema (FBK)

# Table of Content

Abstract .....	8
1 Introduction .....	9
2 Thermo-mechanical degradation modelling.....	10
2.1 Models description .....	10
2.2 CH2P stack geometry, meshing and boundary conditions .....	10
2.2.1 CH2P stack geometry .....	10
2.2.2 Meshing .....	12
2.2.3 Boundary conditions .....	13
2.3 Modelling of the mechanical interactions between the SRU components .....	14
2.4 Simulation procedure .....	15
2.4.1 Stack pre-operation: from anode reduction to stack qualification .....	16
2.4.2 Operation .....	17
2.5 Simulations methodology and results .....	19
2.5.1 Contact pressure loss at the SRU interfaces .....	19
2.5.2 Cell Failure .....	25
2.5.3 Sealing Failure.....	30
2.6 Summary of thermo-mechanical durability modelling .....	33
3 Degradation of the Ni-YSZ electrode microstructure. ....	34
3.1 Microstructural evolution analysis via 3D imaging and characterization.....	34
3.2 Driving forces that affect the stability of the electrode microstructure.....	38
3.2.1 Effect of overpotential .....	38
3.2.2 Effect of oxygen partial pressure .....	39
3.3 Summary for microstructural evolution modelling .....	40
4 Conclusions .....	41
Acknowledgment .....	42
References.....	43

## List of Abbreviations

SP	Partner n°2: SOLIDpower
HTC	Partner n°3: HTceramics
WT	Work Task
EOL	End-Of-Life
SRU	Single-Repeat-Unit
MIC	Metallic Inter-Connect
FEM	Finite Element Method
SOFC	Solid Oxide Fuel Cell
SOEC	Solid Oxide Electrolysis Cell
SOC	Solid Oxide Cell
YSZ	Yttria Stabilized Zirconia
GDC	Gadolinium Doped Cerium
GDL	Gas Diffusion Layer
BCAS	Barium-Calcium-Aluminosilicate glass-ceramic type material
ASC	Anode Supported Cell
ERR	Energy Release Rate
HT	High Temperature
RT	Room Temperature
PZC	Point of Zero Charge

## List of Figures

- Figure 1: Exploded view of the analysed SRU. .... 11
- Figure 2: Overview of the mesh. .... 12
- Figure 3: Schematic view of the mechanical interactions (shown in dashed lines) between the components for “Model v1” (upper) and “Model v2” (lower). Black solid lines ( $\partial\Omega_T$ ): tie contact. Black dashed lines ( $\partial\Omega_{ct}$ ): default non-linear pressure- overclosure relationship. Red dashed lines ( $\partial\Omega_{mct}$ ): modified non-linear pressure-overclosure relationship. Green dashed lines (depicted by  $\partial\Omega$ ): frictionless contact with detachment throughout the whole simulation..... 14
- Figure 4: Overview of the simulation sequence. Points from “A1” to “RT 0 h” comprise the phases of the stack production and qualification, including the first thermal cycle (“A3” to “RT 0h”). Points “HT 0 h” to “HT 150 h” (“Model v1”) and to “HT 10 k h” (“Model v2”) correspond to operation under constant thermos-electrochemical operation, which is followed by a second thermal cycle (“HT 150 h” to “RT 150 h” in “Model v1”, “HT 10 kh” to “RT 10 kh” in the “Model v2”)..... 15
- Figure 5: *Overview of the gPROMS-FLUENT stack thermo-electrochemical model. The developed iterative and flexible interface is indicated by the red arrow (older open-loop in blue). .... 18*
- Figure 6: Evolution of the contact pressure ( $\sigma_{press}$ ) on the anode (left) and cathode (right) sides during stack assembly (A1- A3), thermal cycling (RT 0 h, RT 10 kh) and operation in co-flow with a fraction of pre-reforming of 0.5 (HT 0 h, HT 10 h, HT 10 kh). The temperature profile is shown at the top right. .... 21
- Figure 7: Cumulative density functions of the contact pressure at the interface between (a) the anode and the fuel GDL and (b) the cathode and the air GDL for the four considered operation conditions, at the operating points at RT (end of both first and second thermal cycles), HT 0 h (start of polarisation), HT 10 kh (end of long-term polarisation). Case of ideal MICs, modified periodic boundary conditions, “Model v2” with 0.7 mm sealants. .... 24
- Figure 8: Evolution of the first principal stress ( $\sigma_1$ ) in the anode (GDL-fuel side) and the manifold sealing during stack assembly (A1-A3), thermal cycling (RT 0 h, RT 10 kh) and operation in co-flow with a fraction of pre-reforming of 0.5 (HT 0 h, HT10h,HT10kh)..... 26
- Figure 9: Evolution of the third principal stress ( $\sigma_3$ ) in the YSZ electrolyte and GDC compatibility layer during stack production (A1-A3), thermal cycling (RT 0 h, RT 10 kh) and operation in co-flow with a fraction of pre-reforming of 0.5 (0 h, 10 h, 10 kh). .... 27
- Figure 10: Effect of the operation conditions (co- and counter-flow and varying methane pre-reforming fractions) on the probability of failure computed for a 70-cell stack ( $P_f$ ). Case of ideal MIC with modified periodic boundary conditions (PBC). .... 29
- Figure 11: Elastic energy release rate at the manifold sealants computed by releasing the interfaces without (a) or with frictionless contact (b). Detachment simulations were performed after the first (RT 0 h, black and grey) and after the second thermal cycle (blue: air inlet, red: air outlet) after 10 kh of operation in co-(light blue and red) or counter-flow

with varying fraction of methane pre-reforming. Square and circles refer to FBC and PBC, respectively. Filled and empty markers refer to the interface  $a_1$  (upper) and  $a_2$  (lower), respectively. Thickness of the sealing is 0.7 mm. .... 31

Figure 12: Elastic energy release rate at the manifold sealants computed by releasing the interfaces without (planes with continuous contour) or with frictionless contact (planes with dashed contour). Detachment simulations were performed after the first and second thermal cycle after 10 kh of operation in co-flow and for two sealing thickness (0.2 and 0.7 mm), and varying boundary conditions (EFLT and MPBC). For each condition, only the worst case is shown (corners of the planes, which are provided as a guide). .... 32

Figure 13: *Evolution of measured topological properties (data referred to Table 5.1): (A) total surface areas, (B) interfacial surface areas, (C, D): median phase diameter measured by overlapping spheres (C) and ray tracing (D), density of total and connected TPB (E) and their ratio (F). Measurements on Volumes aged under SOFC and SOEC are shown in red and blue, respectively. The trend lines and error bars are provided as a guide for the eye; the latter were estimated based on measurement of sub-volumes with a size of  $9^3 - 10^3 \mu\text{m}$ . .... 36*

Figure 14: Evolution of the YSZ (A), Ni (B) and pore (C) dihedral angle distributions upon operation. The vertical dashed colour lines are the mean of the distributions, while the black ones are the values measured by Nelson et al. [18], respectively  $97^\circ$ ,  $151^\circ$  and  $111^\circ$ . .... 38

Figure 15: *Computed variation of  $\theta_{Ni}$  under polarization. The maximum value corresponds to  $140^\circ$ . Negative values comport a decrease of the angle therefore higher wettability. The shaded area displays the variation of  $\pm 1$  order of magnitude of the capacitance values. 39*

Figure 16: (left) *Dependence of  $\alpha_{O_2}$  ( $Ni$ ) with  $Ni$  surface tension and  $p_{H_2O}$  (gas). (right) Dependence of  $Ni$  dihedral angle with  $\alpha_{O_2}$  ( $Ni$ ) at  $800^\circ\text{C}$ . Images obtained from [22]. .... 40*

## List of Tables

Table 1: List of selected thermo-electrochemical conditions. ....	19
Table 2: Summary of thermo-mechanical issues severity as a function of the operating mode	33
Table 3: List of volumes used in this study.....	34
Table 4: Metric and topological properties measured on the pristine and aged Ni-YSZ volumes. ....	35

## Abstract

This deliverable presents the activities carried out within the task WT1.5. The objective is to provide in-depth insights and practical recommendations on how to operate the CH2P stack safely under constant conditions and the modulating CH2P modes. For this purpose, a literature review and on-field return of experience made in close collaboration with the technology manufacturer SP have been performed in the frame of task WT2.1 to select the major degradation phenomena that primarily affect the stack efficiency and lifetime. The identified degradation mechanisms can be attributed to two main sources, namely the thermo-mechanical degradation, and the microstructural alterations. These two processes were both investigated by a validated modelling approach in a view to provide practical insights and recommendations for an optimal CH2P stack operation.



# 1 Introduction

The SOFC stack is an in-series assembly of Single Repeating Units (SRUs). The nominal operation of the stack is guaranteed if all the SRUs are structurally intact. Potential mechanical failures in even a single SRU may lead to reduced efficiency and increased degradation in the best case, to temporary interruption of the operation or in the worst case to the End-of-Life (EoL) of the entire stack [1].

Decrease of the contact pressure is reported to increase the contact resistance at the interface [2], which modifies the spatial location of electrochemical reactions. This worsens not only the overall stack performance but also the current density homogeneity, potentially leading to colder zones over the cell active area. Severe thermal gradients and thus high stresses may arise, which may compromise the mechanical integrity of the cell. Then, re-oxidation is likely to occur if cracks propagate to the electrolyte, yielding to parasitic combustion that in turn increases the local thermal gradients. A further decrease of the contact pressure may lead to detachment of the contact interface. In this case, electrical contact cannot be fully recovered.

To the best of our knowledge, the capability to monitor experimentally the structural integrity of the SOFC stack components during operation has not been proven yet. For this reason, numerical thermo-mechanical investigations are of high interest to obtain an in-depth insight of the mechanical behavior of the stack components under different operating conditions. They are thus valuable in understanding and predicting the potential failure modes under CH<sub>2</sub>P operation.

Beside the mechanical issues that a stack can face during operation, on a lower scale the electrodes microstructure can undergo several alterations that may drastically reduce their efficiency or in the worst case cause their EoL if the electronic or ionic charge transfer is compromised. These degradation phenomena mainly affect the fuel porous electrode in Ni-YSZ and its interface with the electrolyte [3]. Up to date, the mechanisms behind these microstructural evolutions remain non-established and the operating conditions that trigger and aggravate them are not clearly understood either.

This work aims at better understanding the mechanical and microstructural degradations that a SOLIDpower stack could undergo under CH<sub>2</sub>P operation. For this purpose, a coupled experimental and numerical approach has been proposed in order to investigate the effect of each operating condition on the stack efficiency and robustness.

This work comes as a direct follow-up of deliverable D2.1 where all the information required to calibrate/validate the proposed thermo-electrochemical and thermo-mechanical models are presented. For an optimal understanding of this deliverable the reader is invited to refer to deliverable D2.1 wherever it is proposed in this report.

## 2 Thermo-mechanical degradation modelling

This section presents the work that has been achieved in order to better understand the mechanical failure mechanisms of a SOLIDpower stack, operating under the modulating CH2P modes. Recommendations are given along this section how to operate the stack in the safest way.

### 2.1 Models description

The stack design analysed in this study is based on the anode-supported cells (ASCs) from the industry supplier SOLIDpower S.p.A (Mezzolombardo, Italy) and is operated within intermediate-temperature range (600-800 °C). It is worth noting that the series of thermo-mechanical investigations presented hereafter use a coupled thermo-electrochemical and thermo-mechanical approach where 3D temperature fields under polarization are simulated using a thermo-electrochemical model for the different CH2P operation modes, and exchanged with a Finite Element Method (FEM) thermo-mechanical model [4–7]. The computational domain is reduced down to a complete SRU, thus taking advantage of the stack geometrical and operating symmetry. In this section, the emphasis is placed on the stack thermo-mechanical reliability with the objective to gain a clearer insight and give practical recommendations on how to operate the CH2P stack in the safest way. From a practical point of view, the thermo-mechanical model was implemented in the commercial FEM code ABAQUS® [8] whereas MATLAB® and gPROMS® were employed for the thermo-electrochemical model and post-processing with some calls to Python routines as well.

Two versions of the thermo-mechanical model are presented in this work. They differ in terms of slight modifications of the geometry, mechanical properties of the material and mechanical interactions between the components. Hereafter, they are referred to as “Model v1” and “Model v2”, respectively.

### 2.2 CH2P stack geometry, meshing and boundary conditions

#### 2.2.1 CH2P stack geometry

The study is focused on the SOFC stack design produced by SOLIDpower. It is worth highlighting that some geometrical modifications have been recently introduced in the newest version of the SOLIDpower SRU geometry which have not been updated in this report. Nevertheless, the present work has been undertaken in a generalisable objective, meaning that the results do not depend on a particular SRU geometry as long as we consider the classical planar design. This has been achieved by making a sensitivity analysis on the stack components geometry, like the cell surface area and the mechanical properties of materials and their interaction, to provide insights and operating recommendations for a large range of stack designs.

An SRU is the elementary item that is piled as many times as needed to obtain a SOFC stack with a target nominal power. The repeating units in a stack are geometrically identical. Thus, with adequate simplifications, a subset of repeating units rather than the entire stack may be modelled to significantly reduce both the computational requirements and the simulation

runtime. With the appropriate set of boundary conditions, the outcome of the stress analysis of a single repeating unit (SRU) will be relevant for a large part of the stack. The geometry of the analysed SRU is shown in Figure 1. The planar ACS is composed of a 270  $\mu\text{m}$  thick NiO/Ni-YSZ anode, a YSZ electrolyte (10  $\mu\text{m}$ ), and an LSCF cathode (40  $\mu\text{m}$ ) separated by a GDC barrier layer (5  $\mu\text{m}$ ). The electrolyte covers the whole area on the upper face of the anode (x-z-plane in Figure 1), whereas the footprint of both the GDC and cathode layers is the same and corresponds to the active area. The inactive area, i.e. the region of the cell that is not covered by the GDC and the cathode, is approximately 4 mm wide. In the SRU model, the cell comprises the anode, electrolyte and compatibility layer, whereas the cathode is not considered. Its stiffness is lower than that of the other cell layers and the cathode layer has therefore a lower effect on the cell curvature and residual stress, compared to that of the other stack components.

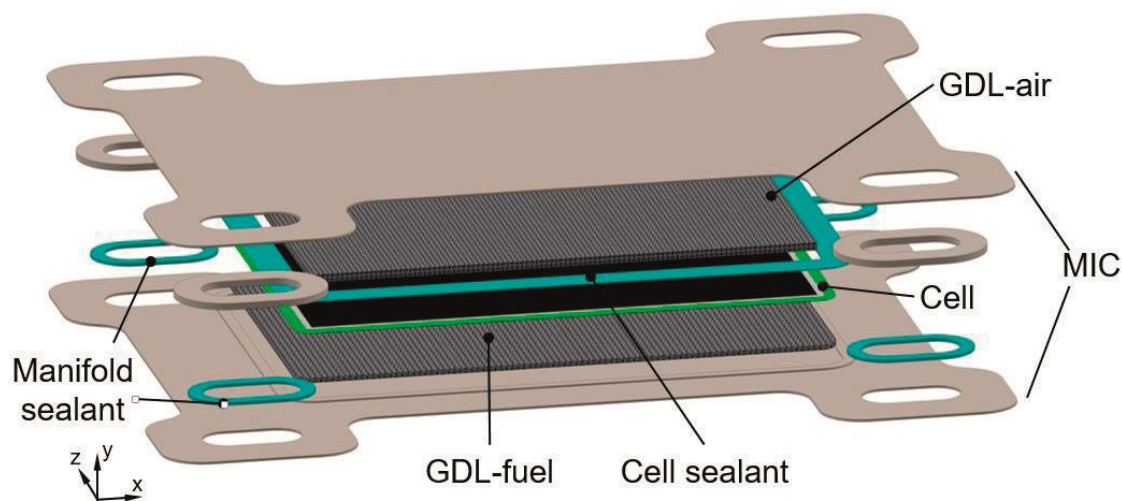


**Figure 1: Exploded view of the analysed SRU.**

This stack design uses an integrated manifold configuration: in co-flow, the two manifolds on the left and right hand side (cf. Figure 1) are respectively the incoming and exhaust fuel streams; the opposite in counter-flow. The air stream is provided externally, from the left to the right hand side of the SRU. To ensure the electrical contact between the MICs and the cell, as well as the distribution of gas over the active area, two pairs of GDLs are inserted, each of them on the two sides of the cell. In the present study, each pair has a first layer in contact with the cell electrodes and another for gas distribution on the MIC side. In Figure 1, the GDL pair on the cathode side is referred to as “GDL air”, whereas that on the anode side as “GDL fuel”. Contact pastes are usually deposited on the contact interfaces of the GDLs before the assembly of the stack. In this work, the mechanical properties of such interlayer with unknown properties were approximated as contact interface instead of solid elements (see Section 2.3 for the details on the numerical implementation).

The repeating unit comprises two sealing geometries to seal the two gas compartments: the cell sealant, joining the inactive area of the cell with the MIC, and the manifold sealants, placed between two contiguous MICs. They are both made of a barium-calcium-aluminosilicate glass-ceramic type material (BCAS).

In “Model v1”, the upper layer of the “GDL air” has the footprint as the active area. This means that the assembly load is supported by the manifold sealants and by the cell active area. To study

the effect of design variations on the stack reliability, the “Model v2” considers a larger “GDL air” plate, which can go in contact with the cell sealant. This entails that part of the assembly load may be supported also by the cell sealant. For further modelling assumptions, discussions are provided in Section 2.3.

The thermo-mechanical properties of the materials in the SRU are listed in D2.1, for “Model v1” and “Model v2”, respectively. The Young’s modulus,  $E_m$ , is mainly dependent upon the porosity  $p$  of the material and temperature  $T$ . The symbols  $\nu$ ,  $\sigma_y$  and  $\epsilon_{red}$  refer to respectively the Poisson’s ratio, yield strength and reduction strain.

## 2.2.2 Meshing

A main effort in the present study was the investigation of the effects of component geometrical imperfections. A workflow, the mesh and modelling assumptions, among others, were developed to perform simulations with idealized as well as geometrically imperfect SRU components. In the idealized case, the model comprises one SRU, to reduce the computational requirements and the simulation runtime. In the second case, two identical SRUs are modelled, to investigate the effects of the component with dissimilar shapes over the two SRUs. The model with one SRU is composed of approximately 350’000 mesh elements, whereas the number of mesh elements is almost doubled for the model with two SRUs. The number of elements may seem low, but the margin for refinement is low for tractable runtime, which are currently in the range of 1-2 days (on 1 node cluster: 14 cores each, 2.2 GHz, 128 Gb RAM), because of the many interfaces. The mesh and the element types used to discretize the components of the SRU models of this work are shown in Figure 2. The rationale behind the choice of the different element types is discussed hereafter.

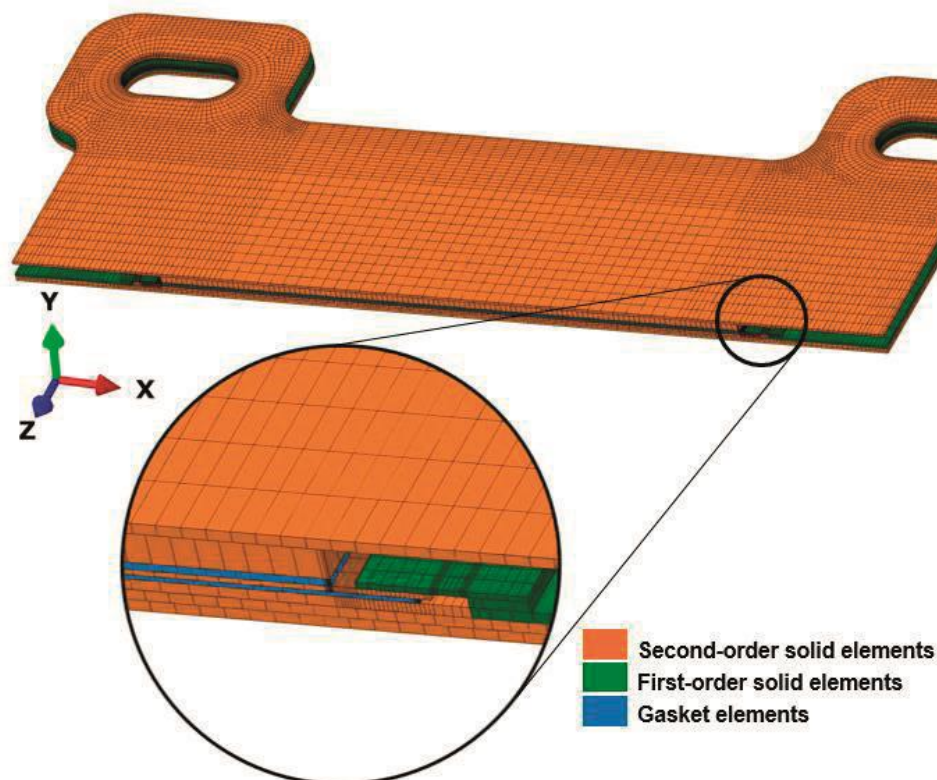


Figure 2: Overview of the mesh.

In this work, the reduction strain of the anode was simulated by imposing an artificial volumetric shrinkage, which requires solid mesh elements. In addition, since the cell bends upon thermal cycling, the use of second-order mesh elements is recommended for improved accuracy of the computed stresses. Hence, the anode was meshed with 3D second-order, reduced-integration solid elements. Simulation tests comprising MIC geometrical imperfections showed that the use of first-order, reduced integration solid elements for both the MICs and the GDLs leads to severe numerical inaccuracies on the computed contact pressure on the active area. The best trade-off between computational requirements and accuracy was obtained by discretising the MIC and the GDL plates (both on the air and fuel sides) with 3D second-order, reduced integration solid elements, whereas 3D gasket elements were used for the second GDL layers. In gasket elements, the in-plane and through-the-thickness mechanical behaviour are uncoupled [9]. Since the GDLs transmit the contact pressure between the MICs and the cell, gasket elements used for meshing such layers must include the through-the-thickness mechanical behaviour. The in-plane mechanical behaviour (also known as membrane behaviour) is included for those GDLs that can withstand shear and tensile/compressive stresses along the in-plane direction caused e.g. by the mechanical interaction with the interfaced components, at the cost of higher computational requirements. In the present two SRU model versions, the gasket elements used to mesh the GDL fuel included both mechanical behaviors, whereas only the through-the-thickness mechanical behavior was enabled for the mesh elements of the GDL air.

### 2.2.3 Boundary conditions

The full stack design considered here typically comprises 70 cells/SRUs. Therefore, two limiting cases were treated to investigate the conditions of units or a cluster of units close to the middle of the stack or to the end plates. The first case is that of a stack made of an infinite number of repeating units, without variations in gas flow among the height, i.e. approximating a real situation where (i) the analyzed SRU is far from the end-plates (ii) the stack is relatively large (iii) the temperature profile is close to symmetric across the z direction and (iv) the loading system can accommodate differences in expansion along the flow path. An intuitive approach for simulating such situation consists in enforcing modified periodic boundary conditions (referred hereafter as PBC) [10,11].

With these boundary conditions, the periodicity of the displacements on the in-plane directions is enforced, whereas the respective nodes on the lower and upper MIC are allowed to rotate around the z-axis. This relative rotation is constrained to be the same for all nodes on which the PBCs are applied. In the case of SRUs, the temperature difference along the gas flow path causes the outlet air side of the stack to be hotter and thus to expand more than at the inlet.

The second case is that of SRUs close to the end plates or approximating a real situation closer to that of a short stack. Oppositely to the case of modified PBC, here the upper and lower MICs of the SRU are enforced to remain flat (FBC), whereas their rotation around the z-axis is allowed.



## 2.3 Modelling of the mechanical interactions between the SRU components

In this study, the mechanical interactions between two or more parts are approximated using either tie or contact. The tie (on surfaces  $\partial\Omega_T$ ) consists in a surface-based constraint, which enforces identical displacements of the mesh nodes of the two surfaces throughout the whole simulation. This mechanical interaction is set to the interfaces between MICs parts and between the MICs and a face of both the GDL air and fuel.

The contact mechanical interaction comprises both a normal and a tangential behavior model. In this study, the normal behavior follows a “softened” non-linear pressure-overclosure relationship. The enforcement of this relationship is approximated by the penalty method, resulting in a contact force that is proportional to the penetration distance, hence allowing a certain inter-penetration of the contacting surfaces.

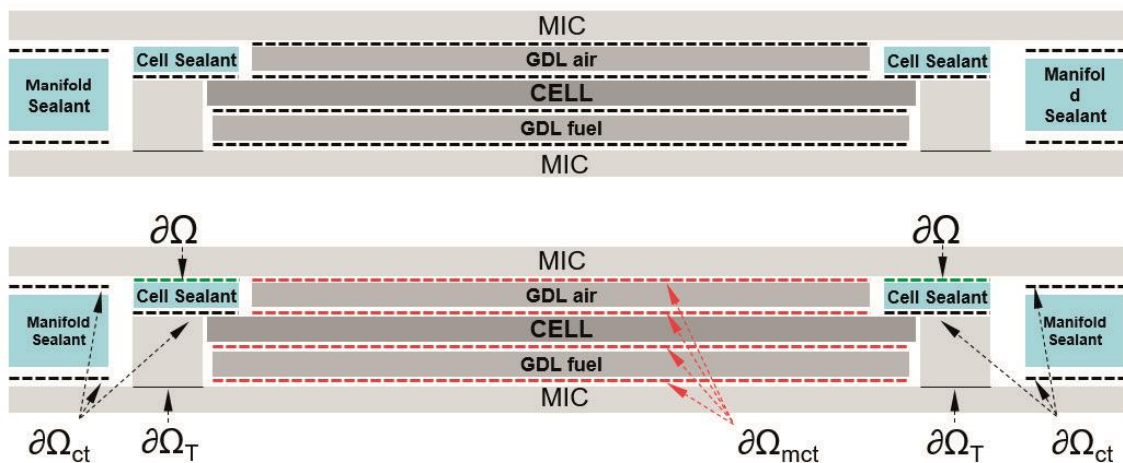


**Figure 3: Schematic view of the mechanical interactions (shown in dashed lines) between the components for “Model v1” (upper) and “Model v2” (lower). Black solid lines ( $\partial\Omega_T$ ): tie contact. Black dashed lines ( $\partial\Omega_{ct}$ ): default non-linear pressure-overclosure relationship. Red dashed lines ( $\partial\Omega_{mct}$ ): modified non-linear pressure-overclosure relationship. Green dashed lines (depicted by  $\partial\Omega$ ): frictionless contact with detachment throughout the whole simulation.**

In practice, the non-linear form of the pressure-overclosure relationship allows a better convergence and an acceptable overclosure as the contact pressure builds up. In both “Model v1” and “Model v2”, the pressure-overclosure relationship does not include separation behavior of the contact surfaces (except for the interface between the MIC and cell sealant, in “Model v2”, see below), to reduce the computational requirements and the simulation runtime. Mechanical contacts were set for the interfaces within the GDLs layers and with the cell active area, between the cell sealant, the cell inactive area and the metallic frame, and for the interface of the manifold sealant with the spacer and the MIC, see Figure 3. In the “Model v2”, the possibility for mechanical interaction between the upper MIC of each SRU and the cell sealant (domain  $\partial\Omega$  in Figure 3) was investigated. This mechanical interaction was modelled by frictionless contact with detachment allowed.

In the present analysis, the sliding between the components in contact is dominated by i) mismatches in thermal expansion and ii) the accommodation of the parts during the assembly

of the stack with pre-deformed (i.e. imperfect, non-ideally flat) components (i.e. the MIC in this study). The magnitude of the relative sliding is expected to be of the same order as the characteristic mesh element length. Under this condition, the small instead of the large sliding formulation is preferred because computationally less expensive. In the small-sliding tracking approach, a local tangent plane on the master surface of the contact pair is associated to the region nearby the slave node. This entails that the contact algorithm does not need to monitor the whole set of slave nodes for possible contact along the master surface [8]. For the tangential contact behavior, the model uses a frictionless sliding approach until the end of the first heat-up. Compared to other works where coefficients of friction of  $0.1\div 0.2$  were used [10,12], this study therefore assumes that interfaces with e.g. contact or sealing pastes do not constrain the relative sliding of the parts in contact. Once the simulated temperature reaches the crystallization temperature of the glass-ceramic sealants, i.e. at the end of the first stack heat-up (see next Section 2.4), a no-sliding condition was enforced for all contact interfaces (except for the interface between the MIC and cell sealant, in the “Model v2”), which aims at simulating the bonding caused by the sintering of both the contact pastes and the glass-ceramic sealants.

## 2.4 Simulation procedure

The SRU thermo-mechanical analyses performed in this work comprise a first set of simulation steps defined as the “initialization sequence”, and a second set where the operating conditions are simulated, i.e. polarization or operation combined with thermal cycling. An overview of the simulation sequence is provided in Figure 4. The presentation of the results is organized using the steps shown in grey in Figure 4, i.e. “A1”, “A2”, “A3” for the assembly, “HT 0 h”, “HT 10 h”, “HT 10 kh” for high-temperature operation under constant thermo-electrochemical conditions, “RT 0 h” and “RT 10 kh”, for cycling to room temperature, for the “Model v2”.

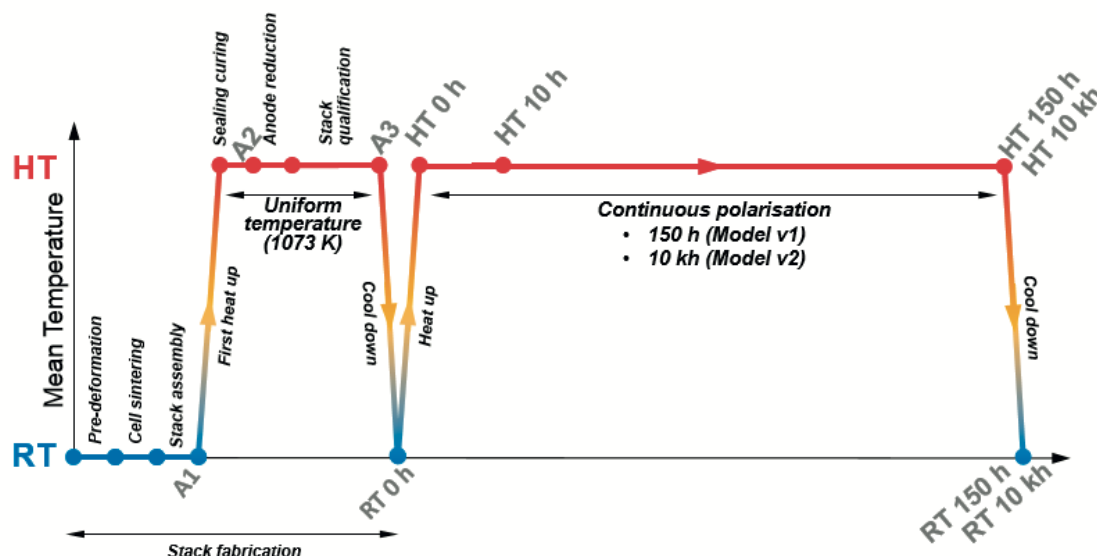


Figure 4: Overview of the simulation sequence. Points from “A1” to “RT 0 h” comprise the phases of the stack production and qualification, including the first thermal cycle (cool-down from “A3” to “RT 0h”). Points “HT 0 h” to “HT 150 h” (“Model v1”) and to “HT 10 k h” (“Model v2”) correspond to operation under constant thermo-electrochemical operation, which is followed by a second cool-down (“HT 150 h” to “RT 150 h” in “Model v1”, “HT 10 kh” to “RT 10 kh” in the “Model v2”).

The sequence is the same for the “Model v1”, except that the simulation duration under constant thermo-electrochemical conditions is shorter (150 h). The simulation time of the initialization sequence for 1 and 2 SRU models was about 15h and 25h, respectively, whereas for the simulation of polarization combined with thermal cycling they are about 20h and 30h, respectively, for 1 and 2 SRU models. These computation runtimes are referred to 1 node cluster, with 14 cores each, 2.2 GHz, 128 Gb RAM.

### 2.4.1 Stack pre-operation: from anode reduction to stack qualification

The initialization sequence aims at calculating the stress in the stack during its manufacturing and conditioning. This sequence comprises both the simulation of real production steps and artificial numerical procedures to approximate the reality. A description of each step is provided hereafter.

**(i) Simulation of components pre-deformation** (=imperfect, non-flat MICs) — At the first step of the initialisation sequence, the position of the upper and lower MICs of the SRU is constrained along the y-axis and the stresses from the MIC model (if the analysis includes pre-deformed components) imported in the homologous components of the SRU model. Since this step is an analysis and not a manufacturing procedure, irreversible deformation (i.e. plasticity and creep) are disabled in all materials using switching of field variables.

**(ii) Cell sintering** — The residual stresses caused by the sintering of the cell layers are reproduced in the stack model by simulating artificial thermal strains. These thermal strains are generated by assigning an artificial CTE for each material of the cell layers corresponding to an increase of the temperature of the whole cell of 1 °C. The reason for this 1 °C increment is the reduction of convergence difficulties because of relative sliding. The artificial CTEs are calculated using an Euler-Bernoulli 1D model [13] including elasticity and creep, which simulates the residual stresses during the cool-down from the sintering temperature of each layer to RT. The artificial CTE of the electrolyte and compatibility layer were computed with respect to the anode. For the present cell, the computed values for the anode, electrolyte and compatibility layer are 0.00, 2.12E-03 and 1.55E-04, respectively. At the end of this simulation step, the CTE of the NiO-YSZ, YSZ and GDC is changed from the artificial to the real values by switching of field variables.

**(iii) Stack assembly force** — The displacement of the MIC along the y-axis is in this step removed, and an assembly force is applied on the SRU. In the model, this force is applied on the stack using multi-point constraint. At the end of this step, plasticity was enabled in all the materials.

**(iv) First heat-up (after point “A1”)** — The stack is heated up from RT to a uniform temperature of 800°C. At the end of this simulation step, the tangential contact behaviour at the contact interfaces depicted by black and red dashed lines in Figure 3 is switched from frictionless to no-sliding condition, for both “Model v1” and “Model v2”.

**(v) Sealants curing** — This step aims at including the change of mechanical properties of the glass-ceramic sealants because of their crystallisation. The dominant change in mechanical properties upon crystallisation is the increase of elastic modulus, from the artificial initial value of 0.2 GPa, up to 14.4 GPa. However, until this simulation step, the sealants in the SRU model are elastically deformed and the strains relatively large (i.e. about 4%, mostly because of the applied assembly force on the SRU as well as to accommodate the pre-deformation of the MICs).



Once the stiffness of the glass-ceramics is increased in the model, relatively high stresses are generated in the sealants and in the interfaced components. These stresses are artificial and are relaxed by simulating artificial creep strains only in the sealants, because in reality the glass-ceramic paste likely deforms plastically until crystallisation. Ideally, at the end of this simulation step, the sealants should be intuitively stress-free, from a macro-scale perspective. In reality, the simulation step is stopped when the stress becomes negligible, e.g. lower than a threshold of 0.5 MPa. At the beginning of this simulation step, creep and plasticity material behaviours are disabled in all materials (except for the creep in the glass-ceramics) and re-enabled at the end of the step, to avoid unrealistic inelastic deformations in the SRU components because of glass-ceramics stiffening.

**(vi) Anode reduction (point “A2”)** — the physical modifications in the anode upon its reduction are the changes in mechanical properties and the shrinkage, which occur together. In this work, the mechanical properties of the anode material are changed from NiO-YSZ to Ni-YSZ by manipulation of the field variables, whereas for the reduction strain and the compensation of the CTE change, with respect to the reference temperature, was applied using artificial isotropic shrinkage.

**(vii) Stack qualification (point “A3”, followed by “RT 0 h”)** — A stack is usually not cooled down right after anode reduction, because of first tests and mild IV-characterization. In the present study, a uniform temperature of 800 °C is maintained for 10 h, during which creep relaxation of the stress in all the SRU parts takes place. At the end of the 10 h, the stack was cooled down to RT. This is the first thermal cycle of the stack.

## 2.4.2 Operation

The baseline case considered in the present study is prolonged operation under the different CH2P modes followed by a thermal cycle. The stress computed by the initialization sequence, i.e. at the end of the first thermal cycle, is used as the restart point for the SRU thermo-mechanical simulations of operation cases, which consists in prolonged continuous polarization in either co- or counter-flow configuration, see Table 1 for an overview of the operation conditions. The hold time under constant polarization differs in “Model v1” and “Model v2”, respectively 150 h and 10'000 h. At the end of the polarization, the stack is cooled down to RT, which represents the second thermal cycle of the stack (point HT 10 kh - RT 10 kh).

A thermo-electrochemical model is used for computing the 3D spatial distribution of temperature in the SRU in operation, for importation into the 3D FEM thermo-mechanical model. The work performed here consisted in implementing the interfaces in MATLAB® for the importation of the temperature profile.

The requirement for the thermo-mechanical analysis is the accurate prediction of the 3D temperature profile, over the range of operation conditions relevant for the SOLIDpower stack. While the local electrochemical model provides local information such as the spatial distribution of electrostatic potentials in the electrolyte as well as single solid phase or composite electrodes, a discussion of the modelling assumptions is outside the scope of this work. In a simplified view, the requirement is here limited to the reasonable prediction of the sink/source terms for CFD

computations. A brief description of the thermo-electrochemical modelling approach is therefore provided hereafter.

The approach consists in coupling a fast thermo-electrochemical model with detailed electrochemistry [5,6] with a 3D computational flow dynamic (CFD) model that comprises adequate level of geometrical detail for the thermo-mechanical simulations. In the active area of the SOLIDpower stack design, the temperature and current density profiles are close to one-dimensional. The modelling approach is based upon this quality. A simplified open loop interface provides a model runtime that allows tractable sensitivity analysis for e.g. meta-modelling [14]. The heat transport and gas flow governing equations are solved in 3D in all domains, except in the cell where the sink/source terms are provided by a finite-difference model, implemented in gPROMS®, an equation-oriented process modelling tool based on the finite-difference/orthogonal collocation on finite-element method.

The information flow is summarized in Figure 5. The transport of electrons and ions and gas species along with chemical and electrochemical reactions is first solved by gPROMS® in all the cell layers, assuming one-dimensional gas and temperature profiles along the air flow direction. The 3D CFD model then solves the transport of mass, heat, and species, with the species and heat source (sink) along the flow direction computed by gPROMS®, after projection and interpolation on the active area of the 3D model. The procedure is implemented in Fluent® by programming User-Defined Functions (UDFs).

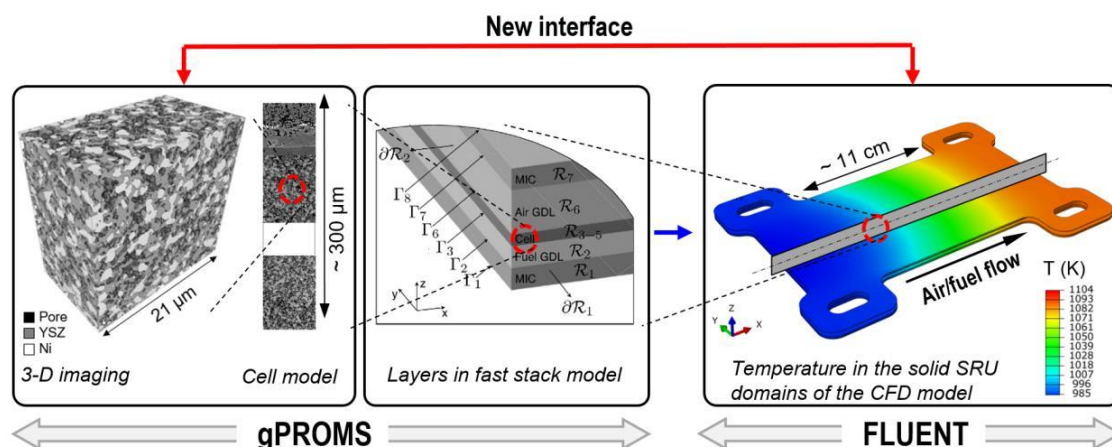


**Figure 5: Overview of the gPROMS-FLUENT stack thermo-electrochemical model. The developed iterative and flexible interface is indicated by the red arrow (older open-loop in blue).**

To reduce complications due to round off errors and interpolation during the importation of the temperature profile into the thermo-mechanical model, the solid parts are modelled with the same level of detail in the CFD and FEM models. Compared to the SRU thermo-mechanical models, the CFD model comprises additional computational domains, such as the thermal insulation and both the air and fuel domains. Periodic thermal boundary conditions are implemented in the CFD model in the y-direction. The compatibility of the meshes between CFD and thermo-mechanical models is facilitated by guaranteeing that the number of cells in the y-direction in the CFD model equals or exceeds that in the thermo-mechanical model, to allow fast 2D interpolation layer-by-layer of mesh nodes in the thermo-mechanical model. Routines were developed for the automatic importation of the temperature profile computed by the CFD

simulations into the thermo-mechanical model. With the implemented gPROMS-Fluent procedure, a simulation requires about 45 min per core (Intel Core i7-3930K) to achieve sufficient convergence. The simultaneous gPROMS® solver allows determining the air flow need to maintain a constant maximum solid temperature in the stack, and constant surface specific power density (including an estimate of the ancillary consumption of the air blower) for investigating the thermo-mechanical effects of differences in features in the temperature profiles.

**Table 1: List of selected thermo-electrochemical conditions. PR = pre-reforming degree of CH<sub>4</sub>**

	PR	U	j	Air ratio	P	S/C	T <sub>air, inlet</sub>	T <sub>max</sub>	FU
	(-)	(V)	(A.cm <sup>-2</sup> )	(-)	(W.cm <sup>-2</sup> )	(-)	(K)	(K)	(-)
Co-flow	0.50	0.74	0.48	5.5	0.33	2	973	1100	0.85
Counter-flow	0.10	0.76	0.47	4.1					
	0.50	0.76	0.48	6.1					
	0.99	0.75	0.49	8.4					

## 2.5 Simulations methodology and results

### 2.5.1 Contact pressure loss at the SRU interfaces

#### *Methodology and Assumptions:*

The interface between the cell and the gas diffusion layers in the active area is central for the stack performance. Achieving and maintaining a low ohmic resistance is not straightforward in a multilayer stack. In a simplified view, a state-of-the-art 70-cell stack comprises more than 500 interfaces that must have the lowest possible resistance to electron transport, among which approximately half have usually low but inaccurately known mechanical properties. The mitigation of imperfect or altered contact is often addressed on a trial and error basis, since predictive approaches have not yet been established. The tolerance on component quality is a first aspect that can be considered, but the experimental identification of the adequate trade-off between performance, durability and costs is far-reaching. Intuitively, the statistical variability in shape and dimensions caused by the manufacturing tolerances is expected to detrimentally affect the uniformity of the contact pressure at the interface. The relationships between the electrical contact resistance and the applied contact pressure were investigated by Dey et al. [2]. They observed that since the cathode has the characteristics of a semiconductor, the contact resistance on the cathode side decreases with increase in temperature. Conversely, the contact resistance on the anode side increases with the increase in operating temperature and is approximately one order of magnitude lower than that of the cathode. The results highlight the dependence between the applied load and the contact resistance. The situation corresponds to that of a sintered screen-printed or tape-cast electrode in contact with a MIC, which therefore depends on the surface quality and cannot be generalized for all stack situations.

The quantitative prediction of the interfacial electrical resistivity in the long-term and under varying operation conditions requires first the knowledge of the contact status and pressure,

and second of the relationship between the contact status and the effective interface conductivity. The present studies are focused on the first aspect. Therefore, there is no feedback from the thermo-mechanical simulation results to the thermo-electrochemical mode.

From the mechanical standpoint, the phenomena that can result in a history-dependent contact status in the model are the effect of history on the stress state, in a simplified view. In contrast, the possibility for the damage of the contact interfaces is not simulated. This is because the contact formulation allows any region of discretized surface, that underwent zero or tensile contact pressure or opening, to fully recover its original contact properties at any time, which is unlikely the case in reality.

Contact issues differ whether the anode/GDL-fuel or the cathode/GDL-air interface is considered: the cathode has a lower electric conductivity and thickness than the anode, therefore the effects of current constrictions at the scale of the interconnection system are more severe on the cathode/GDL-air interface [10]. Post-test disassembly further shows that the strength of the cathode side interface is also lower. In the present study, both contact interfaces are investigated. The contact pressure computed by Abaqus® is positive, or negative, if the interface is under compressive, or tensile, stress respectively.

The evolution of the contact is quantified by computing the probability density function of the contact pressure at the interfaces. The binning of the contact pressure data is performed using as weight the corresponding element surface area.

The “Model v1” and “Model v2” comprise 2 repeating units for the analysis of the pre-deformation profiles “2Def00”, “2DefA” and “2DefB”. The spatial distribution of the contact pressure is not identical within the two pairs of cathode or anode interface. For comparison with the reference 1 repeating unit model, the equivalent contact pressure is calculated for each mesh element on the same interface of both SRUs. This post-processing choice therefore places the emphasis on the probability of interface separation at either one or both SRUs, which may cause alteration of the electrical field. The discrepancy in contact pressure within pairs of same GDL is of interest, but not discussed quantitatively using a dedicated metric. It is analyzed qualitatively by visual comparison of the computed contact pressure spatial distributions.

### *Results:*

The contact pressure simulated at the interface between the cell and the fuel and air GDLs is shown in Figure 6. The contact pressure on both interfaces is the combination of both the assembly force and interaction with the manifold sealants.

As expected and desired, the spatial distribution of the contact pressure computed for the cathode side mostly mirrors that for the anode side. The slight variations near the cell edges are due to the mechanical interaction with the cell sealing.

The contact pressure on the active area after the application of the assembly load is about 0.48 MPa ( $\sim 4.8 \text{ kg/cm}^2$ ). Under these conditions, the manifold sealants are in mild traction. This situation is a modelling artefact, because the pressure-overclosure relationships in “Model v2” include a clearance at zero contact pressure, which causes an artificial opening of the contact interfaces on the active area between the GDLs, cell and MICs. The contact pressure at the

interface between manifold sealant and MIC at the condition A1 is about -5 MPa (interface in traction).

After the sealants curing in the initialization sequence (see Section 2.4.1), the artificial creep strain relaxes the stresses in the manifold sealants, leading to a contact pressure at the interface between the manifold sealant and MIC of about -2 MPa (interface in traction). This reduction is also due to a modification of assembly force (see Section 2.4). In these conditions, the contact pressure on the active area was 0.31 MPa. In the point A3, i.e. after anode reduction and 10 h at 1073 K, creep relaxed further the artificial stresses in the manifold sealants, and the contact pressure on the sealants became about -1.5 MPa. In these conditions, the contribution of tensile stresses in the manifold sealants on the contract pressure on the active area is still not negligible, i.e. the contact pressure on the active area (about 0.19 MPa) is supplied both by the manifold sealants and by the assembly force. Contact pressure simulated in steps A1-A3 are therefore an overestimation of the reality, but the main outcome is that the design does not result in strong heterogeneity of the contact pressure in the contact area during the assembly and heat-up, despite the bending of the SRU (see Section 0), which is beneficial for the last step of the stack fabrication.

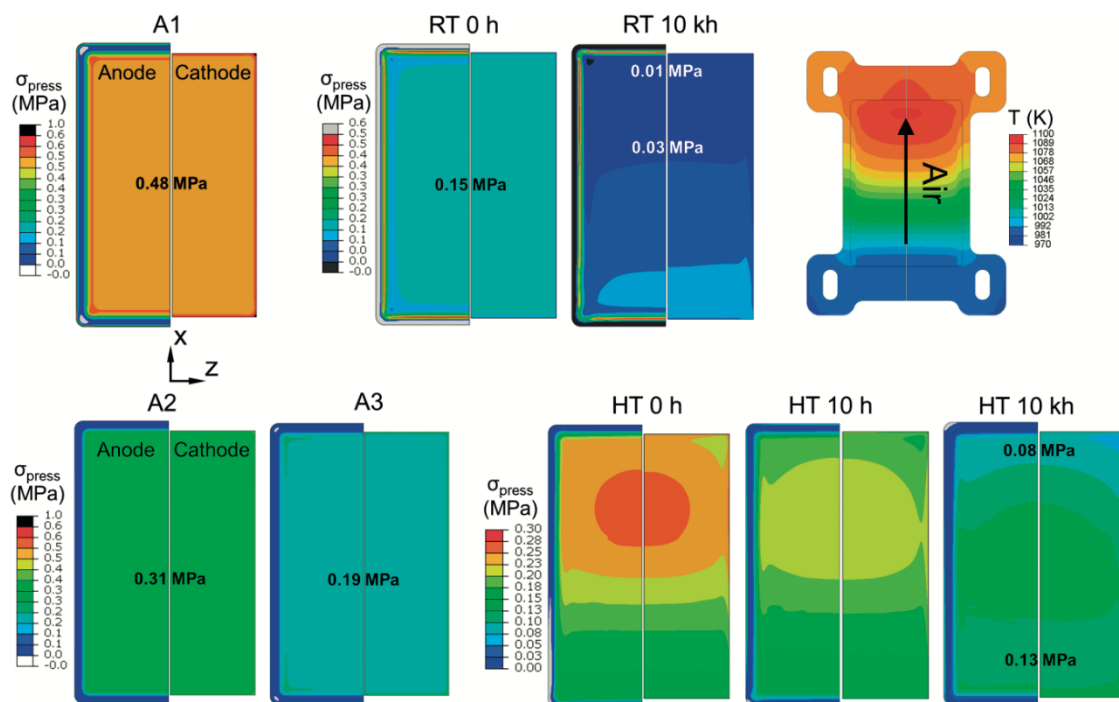


**Figure 6:** Evolution of the contact pressure ( $\sigma_{press}$ ) on the anode (left half of cell) and cathode (right half of cell) during stack assembly (A1- A3), after cool down (RT 0 h, RT 10 kh) and after operation in co-flow with a degree of pre-reforming of 0.5 (HT 0 h, HT 10 h, HT 10 kh). The temperature profile is shown at the top right.

After the first cool down to RT, the contact pressure on the active area (on the manifold sealants) decreases (increases) from 0.19 to 0.14 MPa (from -1.5 MPa to -0.8 MPa). These variations are caused by the CTE mismatch between the glass-ceramic (i.e. the manifold sealants), the GDLs and the cell. Assuming that at the point A3 (1073 K) the thickness of the manifold sealant is equal

to the sum of the thicknesses of both GDLs and cell, upon cool down to RT (point: RT 0 h) the GDLs shrink by a larger amount than the sealant.

Since the assembly force on the stack remains unchanged, the different thermal shrinkages caused the contact pressure to decrease on the active area (see Figure 6) and to increase on the manifold sealants. Regions of high contact pressure (in Figure 6, the red ribs of about 0.5 MPa) are found on the edges of the anode contact interface, after both the first and the second thermal cycles. This is ascribed to a change in cell curvature in the inactive transition region between the active and sealing area, because the upwards bending of the cell upon cool down is constrained on the inactive area by the cell sealant.

Upon polarization in co-flow, the thermal expansion of the GDLs is higher than that of the manifold sealants at both the air inlet and outlet regions, because i) the CTE of the GDLs materials are higher than that of the glass-ceramics and ii) the active area is hotter than the manifold regions. These two contributions control the contact pressure on the active area upon polarisation, because in comparison with the condition A3 (uniform temperature of 1073 K) the contact pressure increases at the outlet (i.e.  $T > 1073$  K), whereas it decreases at the inlet (i.e.  $T < 1073$  K). However, the zones of highest contact pressure at HT 0 h do not correspond to the highest temperature, because of the trade-off between the decrease of the elastic properties with the temperature increase and higher contact pressures for larger mismatches of thermal expansion. In these conditions, the contribution to the higher contact pressure at the outlet is given in part by the assembly force, and in part by the manifold sealants in tension. Upon long-term polarization, creep in both the glass-ceramic and in the GDLs materials, among others, monotonically relax both the compressive stresses in the GDLs and the tensile stresses in the manifold sealants. The decrease of contact pressure is significant in the first 10h of polarization, see point HT 10 h in Figure 6. However, this decrease would be expected faster if primary creep was included in all the material constitutive laws of the SRU model.

Because of the strong dependence of the creep strain rate on the temperature, the contact pressure decreases more rapidly near the air outlet than the inlet region: after 10 h of polarization, the contact pressure at the outlet is already similar to that at the inlet. In the long-term i) the higher creep strain rates because of the higher temperature lead to contact pressure at the outlet region lower than at the inlet, i.e. the opposite pattern from the start of the polarization (point: HT 0 h), and ii) the mean contact pressure on the active area would converge to the value given by only the assembly force without the effect of the sealants, around 0.12 MPa.

After the second cool down (point RT 10 kh) the contact pressure decreases, for the same reasons as in the first thermal cycling (point: RT 0 h). However, the contact pressure before the cool down was lower in HT 10 kh than in A3. As a result, after the second thermal cycle the contact pressure in RT 10 kh was almost lost on a large region of the active area. This showcases an undesirable situation, because the region affected first by a loss of contact pressure corresponds to that of highest current density. Compared to RT 0 h, the contact pressure is also less uniform at RT 10 kh. The reason is that, similarly to the heat-up for the start of polarization (point: HT 0h), the difference in thermal shrinkage upon cool down between the GDLs and the manifold sealants is larger at the outlet, because the outlet of the active area is hotter than the

inlet. As a result, the outlet region is at lower contact pressure than at the inlet, and the manifold sealants support about 80% of the assembly force.

The simulations indicate that ensuring a constant and uniform contact pressure at the interface between the cell and GDLs is a challenge. The effect of history is observed and suggests that the risk of contact issue can be expected to increase upon operation, during thermal cycling.



### Effect of Operating Conditions:

The effects of variations in the operation conditions on the distribution of the contact pressure at the interfaces between the anode and the fuel GDL and between the cathode and air GDL are shown in Figure 7 for the points HT 0 h (start of polarization), HT 10 kh (end of long-term operation) and RT (thermal cycle at the end of long-term polarization).

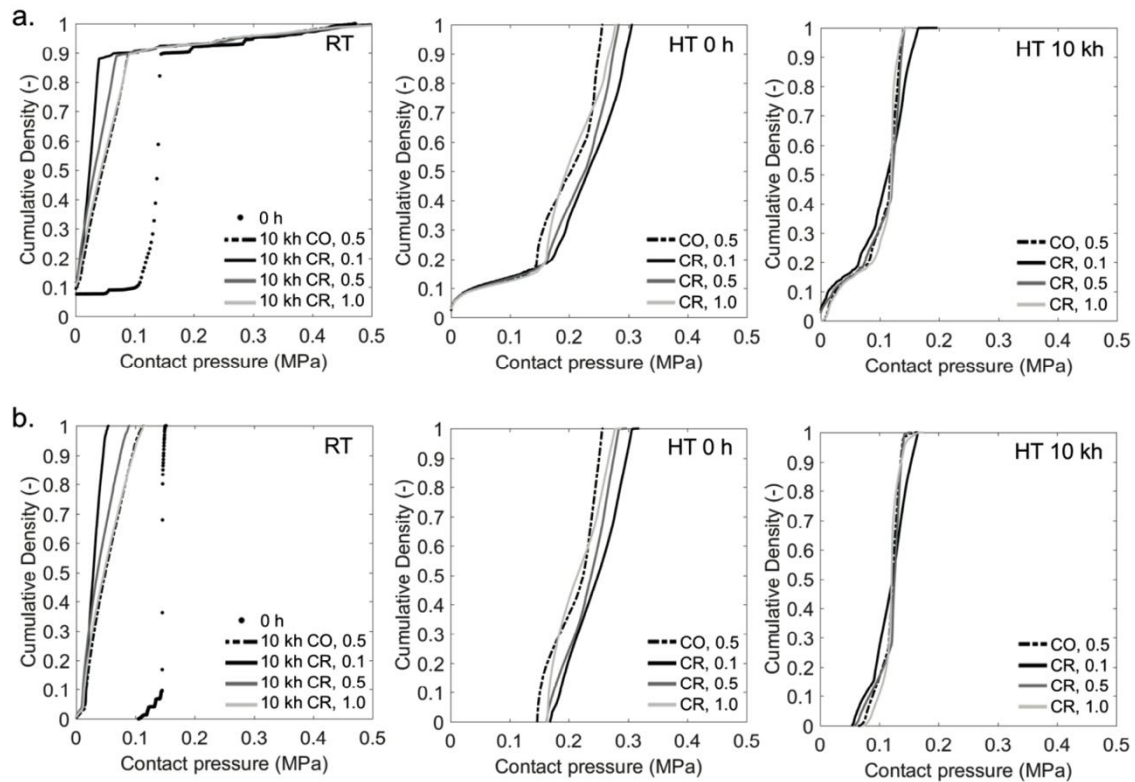


**Figure 7: Cumulative density functions of the contact pressure at the interface between (a) the anode and the fuel GDL and (b) the cathode and the air GDL for the four considered operation conditions, at the operating points at RT (end of both first and second thermal cycles), HT 0 h (start of polarisation), HT 10 kh (end of long-term polarisation). Case of ideal MICs (perfectly flat, non-deformed), modified periodic boundary conditions, “Model v2” with 0.7 mm sealants.**

The cumulative distribution of the contact pressure distribution for the RT 0 h is shown as reference in the RT plots in Figure 7. Since upon heat-up the cell deflection decreases and the thickness of the GDL-fuel increases because of thermal expansion, the contact pressure between the inactive area of the cell (constrained by the cell sealant) and the GDL-fuel is partially recovered, compare plots for the anode side between RT and HT 0 h for values of the contact pressure close to zero. Since the temperature is uniform until the point RT 0 h, the contact pressure on the active area is practically homogenous.



*Summary:*

In this study, the contact pressure simulated by “Model v1” (with ideal MICs) was largely lost, compared to the “Model v2”. Paradoxically, the assembly force in the “Model v1” simulations was about 33% higher than in “Model v2”. Here, the contribution of both the mechanical properties of the GDLs and SRU deformation on the maintenance of the contact pressure was found highly relevant, because in “Model v1” the GDL mechanical properties were estimated by simple scaling laws, whereas computational homogenization of anisotropic elastic and creep properties was used for those of “Model v2”. This significant difference indicates that the design of the GDLs can be optimized not only for fluid-dynamic and cost needs, but also for improved mechanical behavior. In this context, thermo-mechanical simulations at the stack level may help in providing guidelines for such optimizations. For “Model v1”, the worst condition was the thermal cycling. Instead, stack qualification and polarization were found beneficial.

**2.5.2 Cell Failure***Methodology and Assumptions:*

For the computation of the failure probability in the anode, the Weibull statistics parameters of NiO-YSZ and Ni-YSZ obtained from four-point bending tests and at room and high temperature are used (cf. D2.1). Confidence intervals on the failure probability are computed using the lowest and upper bound of the 90% confidence interval values on Weibull modulus, characteristic strength and reference volume.

The probability of failure is computed by integration over the volumes of the mesh elements of the cell layer, following the standard expression assuming the principle of independent action:

$$P_{f,i} = 1 - \exp \left\{ - \frac{1}{V_0 \cdot (\sigma_0)^m} \cdot n_{cells} \cdot \int_{V_i} \left[ \sum_{ps=1}^3 (\sigma_{ps})^m \right] dV_i \right\} \quad (1)$$

where  $V_0$  is the reference volume,  $m$  the Weibull modulus,  $\sigma_0$  the characteristic strength of the material,  $n_{cells}$  the number of cells in the stack and  $\sigma_{ps}$  the principal stress with  $ps = 1, 2, 3$  which indicates the first, second and third component of the principal stress. The integral can be evaluated for each volume of material  $i$  in the SRU, with  $i$  = anode, electrolyte, compatibility layer. Only positive (tensile) values of the principal stress are used for calculating the probability of failure.

The Weibull parameters measured in WT2.1 and usually found in the literature correspond to the strength for the pristine material. Microstructural changes were observed for the present anode under SOFC operation. An effect on the strength cannot be excluded. Therefore, the direct comparison of the simulations at the start and end of operation requires some care. The analysis based on computational homogenization in WT2.1 however shows that the change in the thermo-elastic properties due to changes in the morphology and topology are limited. The variations in the strength are therefore likely limited if the degradation does not affect the volume fraction of the phases.

### Results:

The overall trends observed in the evolution of the stress in the cell layer during the simulated sequence shown in Figure 4 are discussed. The 1st principal stress computed in the anode is shown in Figure 8. The effect of i) the anode reduction and ii) the constraint of the sealant and GDL-fuel on the cell leads to relevant changes in the stress in the anode between the points A1 (stack assembly) and RT 0 h (i.e. end of the first thermal cycle). The computed stress state in the anode evolved from tensile (about +20 MPa) to stress-free condition. The stress state at the end of the first and second thermal cycle (points RT 0 h and RT 10 kh, respectively) also remains similar. This result indicates that the effects of thermal cycling dominate that of history during long-term polarization. From a material viewpoint, the stress state in the anode is less affected by creep than by the mismatch in CTE between the cell and the other stack components.

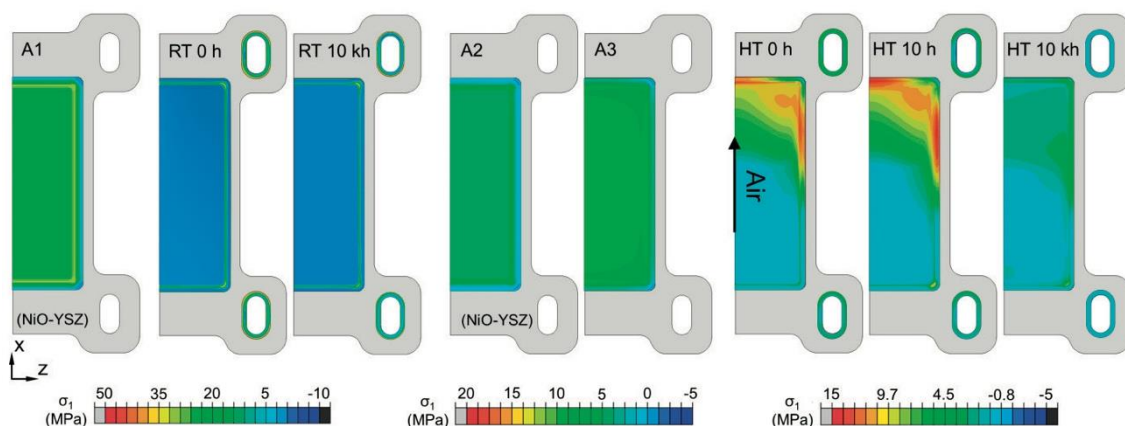


**Figure 8: Evolution of the first principal stress ( $\sigma_1$ ) in the anode (GDL-fuel side) and the manifold sealing during stack assembly (A1-A3), after cool down (RT 0 h, RT 10 kh) and after operation in co-flow with a degree of pre-reforming of 0.5 (HT 0 h, HT10h, HT10kh).**

The first principal stresses in the active area of the anode increase upon reduction (points A2 and A3, respectively for anode in oxidized and reduced state), from about +5 MPa to +9 MPa. This stress increase is caused mostly by the interactions with the joined parts (i.e. the GDL-fuel and the MIC, on the lower side, and the electrolyte with the compatibility layer, on the top side) and the isothermal shrinkage of the anode. Conversely, in the inactive region of the anode, the constraint of the GDC is not present, hence the increase of stress is less pronounced.

Under polarization, the stress state in the anode is a modulation of the point A3 by the inhomogeneous spatial temperature distribution. Compared to A3 (uniform temperature of 1073 K), the region at the air outlet (inlet) is higher (lower) in the point HT 0 h, i.e. at the start of the polarization in co-flow. Because i) of the constraint of the anode with the GDL-fuel and ii) the CTE of the GDL-fuel material which is higher than that of Ni-YSZ, the higher thermal expansion of the GDL-air was constrained by the anode. Hence, since the inlet region is colder at the point HT 0 h than in A3, the tensile stresses in the anode are lower. The higher tensile stresses, i.e. at about +15 MPa, are located in the cell inactive area surrounding the hottest region of the temperature profile in co-flow (see Figure 8). The reason is that the surrounding inactive area is colder, and thus constrains the higher thermal expansion in the active area.

Creep does not yield a monotonic relaxation of the stress in the anode. At the operation point HT 10 h, the first principal stress in the anode first increases, since the SRU bent downwards as a consequence of the different in-plane creep strain rates in the bonded components, and this increased the stresses in the lower face of the anode. Over the long-term, the stress in the anode is however relaxed. The creep strain rate depends on stress and temperature.

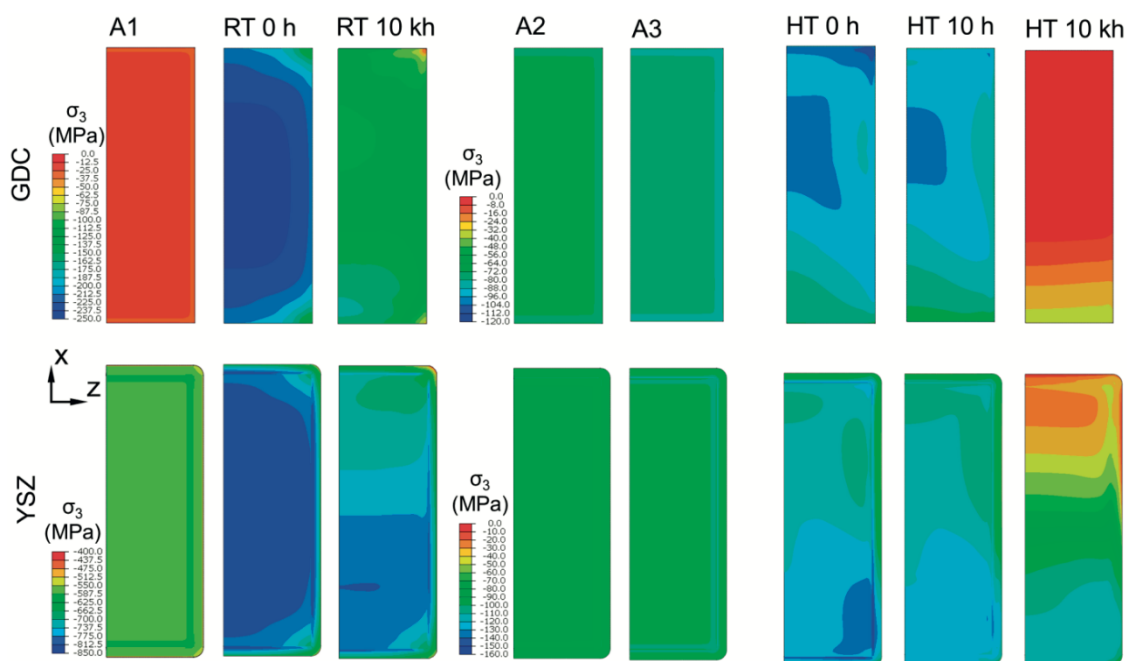


**Figure 9: Evolution of the third principal stress ( $\sigma_3$ ) in the YSZ electrolyte and GDC compatibility layer during stack production (A1-A3), after cool down (RT 0 h, RT 10 kh) and after operation in co-flow with a degree of pre-reforming of 0.5 (0 h, 10 h, 10 kh).**

Therefore, the larger stress relaxations occurred in the regions of highest stress and temperatures over the long-term polarisation, which are on the air outlet side. In the ASC configuration, the thin YSZ and GDC are subjected to compressive shielding stress. Figure 9 provides an overview of the effects of i) the assembly process (A1, A2 and A3) and ii) long-term polarisation in co-flow (HT 0 h to HT 10 kh) and iii) thermal cycling (RT 0 h and RT 10 kh) on the third principal stresses in the electrolyte and in the compatibility layer.

After the cell sintering (point A1 in Figure 9), both the electrolyte and compatibility layer are under compressive stresses, of about -600 and -20 MPa, respectively. The increase in tensile stress in the anode upon its reduction (stress states A2-A3 shown in Figure 8) is compensated by a limited increase of the compressive stresses in both the electrolyte and compatibility layer, by comparing the stress state in points A2 and A3.

Upon polarisation, the compressive stresses decrease (increase) in the electrolyte (compatibility layer) in the hottest region of the cell (i.e. at the outlet), see point HT 0h in Figure 9. The effects of creep are relevant already during the first 10 h of polarisation. Then, the compressive stresses in both layers are largely relieved during the long-term polarisation, see point HT 10 kh in Figure 9. In this situation, the compatibility layer is under compression only in a restricted region at the inlet, where creep strains were limited by the lower temperatures, whereas the rest of the layer undergoes very low tensile stresses (red region in point HT 10 kh in Figure 9). On the contrary,

the compressive stresses in the electrolyte are not completely relieved after the 10 kh under polarisation.

Since the CTE of Ni-YSZ is higher than that of both YSZ and GDC, the higher thermal shrinkage of the anode upon cool down (i.e. from A3 to RT 0 h, and from HT 10 kh to RT 10 kh) results in beneficial compressive stresses in the electrolyte and the compatibility layer for the RT conditions. The magnitude of the stress is however lower than initially.

The simulated tensile stress in the anode is low and not expected to lead to a high initial probability of failure, or long-term problems since microstructural analysis suggests that the mechanical properties are expected to vary mildly upon aging. From a proof-testing perspective, the pattern of the stress in operation does not change significantly and while the magnitude of the stress increases during the beginning of operation, a strong dependence on operation history is not observed for the simulated conditions. The decrease of the shielding stress in the YSZ electrolyte and GDC compatibility layer is in contrast detrimental, but the present analysis does not highlight a critical situation. The results however suggest that the vulnerability towards re-oxidation or rapid changes in operation conditions may be practically lowered.

#### *Effect of Operating Conditions:*

Figure 10 provides a comparison of the probability of failure of the anode computed for the four cases of polarization analyzed in this work, followed by cool down to RT. The “Model v2” is here considered, with PBC and with ideal MIC. A relevant aspect is the location of the region of highest temperature in the cell, because the cell regions surrounding the hottest zone constrain the higher thermal expansion and thus are subjected to tensile stress. Therefore, the operation with the conditions CR 0.1 (counter flow, low degree of pre-reforming of 10%) is the most critical, yielding a probability of failure between 0-1. In the long-term, creep relaxes the stresses in all materials. Since the creep strain rate is strongly dependent upon temperature and stress, the stress relaxation is the highest under the conditions CR 0.1. As a result, the cell failure probability for this polarization condition is reduced drastically after 10 kh of operation, which even turns out being the safest condition among the conditions shown in Figure 10.

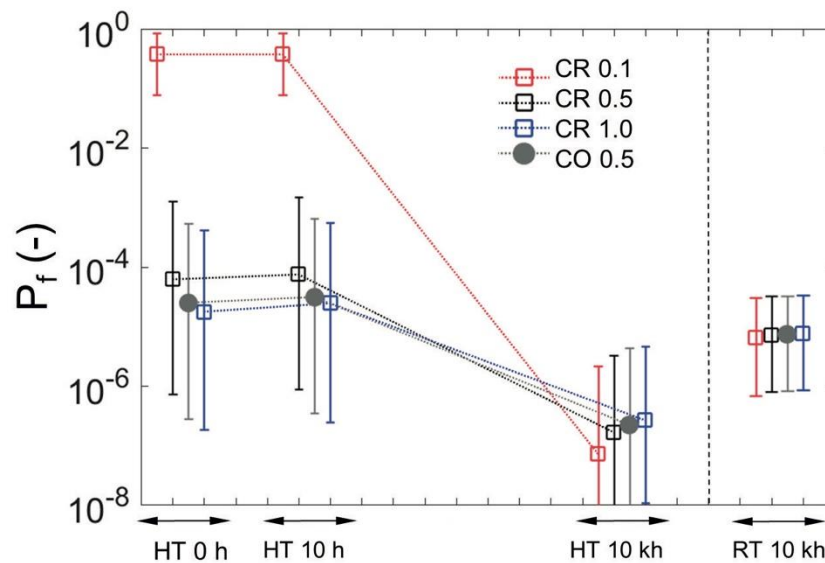


**Figure 10: Effect of the operation conditions (co- and counter-flow and varying methane pre-reforming degrees of 10, 50, 90%) on the probability of failure computed for a complete 70-cell stack ( $P_f$ ). Case of ideal MIC with modified periodic boundary conditions (PBC).**

#### *Summary of Cell Failure:*

The cell reliability is highly affected by the CH2P operating modes. The failure probability increases dramatically if the fraction of internal reforming is very low (with counter-flow configuration). In terms of cell reliability, counter-flow configuration with 10% of internal reforming is the worst condition among those analyzed in this study, because it leads to failure probabilities higher than 0.1 in the short-term polarization, which is not suitable for practical applications. However, after long-term polarization this became the best condition. The sensitivity of the anode failure probability to the polarization conditions is predominant for high degrees of internal reforming: by increasing the PR (in counter-flow) from 0.1 to 0.5, the cell failure probability is reduced in the short-term polarization by almost four orders of magnitude. The results suggest that the effects of transients during load following or variations in thermal conditions because of the position in the stack are likely significant.

Cooling down after long-term polarization increases the risk of cell failure. However, the probability remains relatively low. Here, as expected, a reduction of the CTE mismatch between the glass-ceramic and Ni-YSZ by tailoring of the material compositions would increase the tolerance of the cell to thermal cycling.

With the deformation profiles considered in this work, the effects of MIC pre-deformations on the risks of cell failure are negligible. The reason was that the compliance of both the cell and GDLs was sufficient to accommodate the deformed components (i.e. imperfectly flat MICs). Considering this aspect, thinner cells are favored, because they can tolerate larger component imperfections before failure.

### 2.5.3 Sealing Failure

A technological difficulty with ceramic materials is that they tend to be much more brittle compared to metals. Therefore, the effects of geometrical and material singularities that trigger damage by cracking, because of localized high stress that exceeds the strength of the material [15], must be investigated. Failure occurs in the elastic deformation regime with limited possibility for plastic deformation at the crack tip, which entails that the crack process zone is negligibly small. The analysis of failure in ceramics therefore typically starts with Linear Elastic Fracture Mechanics (LEFM) theory. The fracture mechanics problem has been historically tackled from two perspectives provided by stress or energy balance of a system comprising a pre-existing crack.

The stress intensity approach is based upon the analysis of the stress field near the crack tip. The inspection of the analytical solution for the stress field derived by Irwin [16] shows that each component of the stress tensor is proportional to a constant, which therefore represents a stress-intensity factor. The analysis holds for different loading, referred to as Mode I (opening), Mode II (sliding) and Mode III (tearing), which yields the stress intensity factors  $K_I$ ,  $K_{II}$  and  $K_{III}$ . Failure corresponds to a critical stress intensity factor, which is a measure of the material resistance.

The concept in the energy balance approach introduced by Griffith roots from the first law of thermodynamics, i.e. crack extension occurs when the energy available in the system exceeds the resistance of the material, because energy is required to break the atomic bonds. The nature of the relevant processes that dissipate energy upon crack extension differ depending on the material, but for evident reasons, always comprise the generation of new surfaces. The energy balance for an infinitesimal crack growth provides the energy release rate (ERR), which must exceed a critical value that is a measure of the toughness of the material.

The inspection of the expressions derived from the energy and stress analysis approaches for a crack in the bulk of a linear elastic material, yields a relationship between the energy release rate and stress intensity factor, indicating that for such a case the two approaches are equivalent.

A simplified approach based upon energy considerations has been implemented as a post-processing procedure of the stack simulations to inform qualitatively and comparatively about the risk of failure of the sealant. The calculation of the ERR consists in the variation of the stored elastic strain energy between far behind and upfront the crack tip position, i.e.:

$$G_{SS} = U_{el}^{III} - U_{el}^I \quad (2)$$

#### Results:

An overview of all the ERR estimated by surface detachment in the stack “Model v2” is provided in Figure 11. The analysis based on the implemented procedure for ERR estimation and on stress cumulative distribution function differs. The variations observed among the cases are much more significant than for the stress-based analysis.



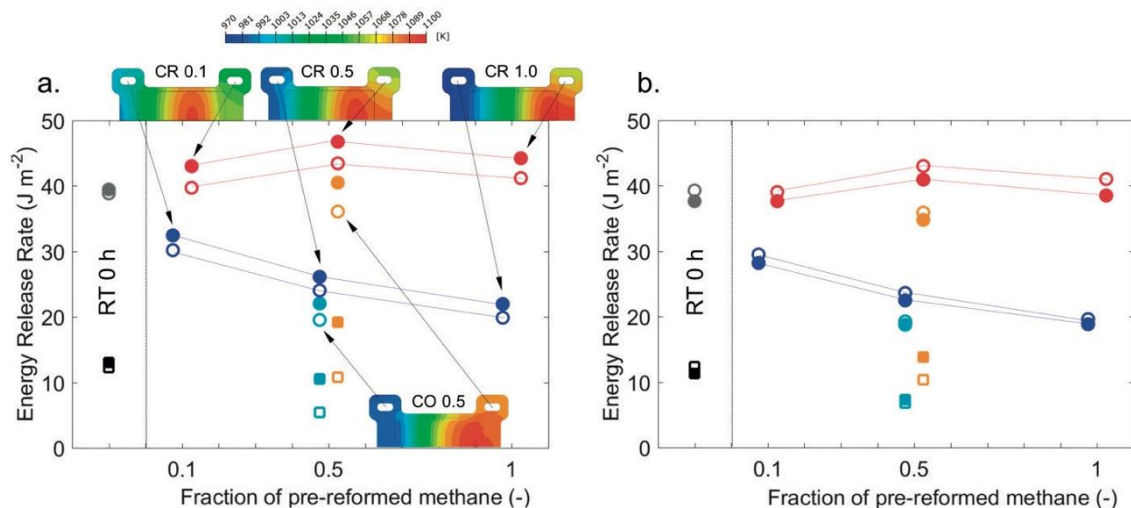


**Figure 11: Elastic energy release rate at the manifold sealants computed by releasing the interfaces without (a) or with frictionless contact (b). Detachment simulations were performed after the first (RT 0 h, black and grey) and after the second thermal cycle (blue: air inlet, red: air outlet) after 10 kh of operation in co-(light blue and red) or counter-flow with varying degree of methane pre-reforming. Squares and circles refer to FBC and PBC, respectively. Filled and empty markers refer to the interface  $a_1$  (upper) and  $a_2$  (lower), respectively. Thickness of the sealing is 0.7 mm.**

As a first verification, the calculated ERR is practically the same for the inlet and outlet manifold sealants after the first thermal cycle. The computed discrepancy is lower than 0.5 % in the worst case. The range of ERR values calculated with interface detachment of 0.7 mm thick sealant after the first and second thermal cycle is 10-35  $\text{J m}^{-2}$ , which falls within the same range as the VCCT values (virtual crack closure technique criterion for linear elastic fracture) both with stripe and axisymmetric geometries, approximately 10-50  $\text{J m}^{-2}$ . The difference in the geometry likely accounts for a non-negligible share of the difference. The ERR computed for the FBC is in average about three times higher than for the PBC case, which suggests that the risk of sealant failure is dependent upon the position in the stack.

The case without frictionless sliding is first discussed (Figure 11-a). The ERR calculated for the interface  $a_1$  (upper) is higher than for  $a_2$  (lower) by about 6% and 2%, respectively with FBC and PBC, which is qualitatively in line with the VCCT on axisymmetric calculations. For all polarization cases, the ERR calculated with interface detachment is always higher at the air outlet than at the inlet manifold sealant. Operation in counter flow proves more critical after the second thermal cycle, based on the case PR=0.5. For all counter-flow cases (PR=0.1, 0.5 and 1.0 and PBC), the ERR of the outer manifold sealant is higher than after the first thermal cycle, for both interface  $a_1$  and  $a_2$ , whereas at the inlet it is lower. The most critical case is CR 0.5, with an increase in ERR by about 20% compared to the first thermal cycle. The results suggest a detrimental effect of long-term operation, which is not clearly highlighted by the stress-based analysis. In reality, the properties of the interface are further expected to change and contribute to additional time and history dependence.

In co-flow with PR=0.5 and PBC, the ERR increases (decreases) by about 4% for interface  $a_1$  ( $a_2$ ) after the second thermal cycle. For the same operation conditions but in FBC, the ERR increases at interface  $a_1$  by about 40% compared to the first thermal cycle. Hence, after the second thermal cycle the interface  $a_1$  (upper) is more critical than  $a_2$  (lower).

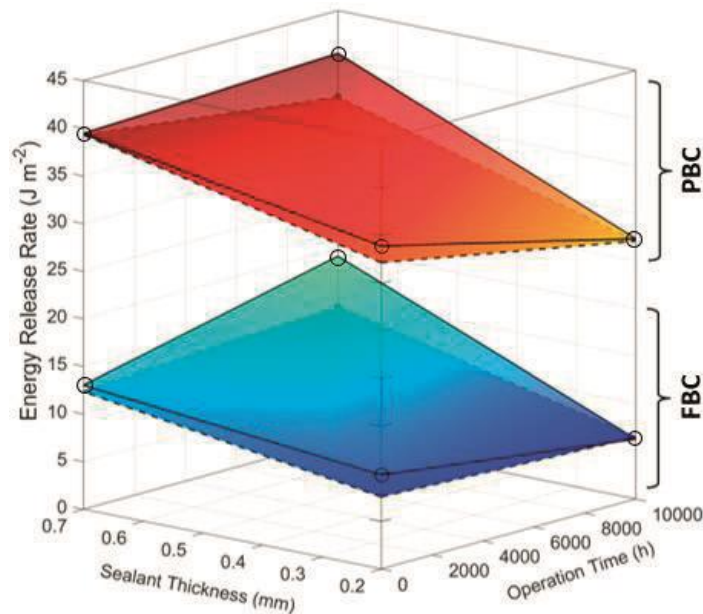


**Figure 12: Elastic energy release rate at the manifold sealants computed by releasing the interfaces without (planes with continuous contour) or with frictionless contact (planes with dashed contour). Detachment simulations were performed after the first and second thermal cycle after 10 kh of operation in co-flow and for two sealing thickness (0.2 and 0.7 mm), and varying boundary conditions (Flat and Periodic Boundary Conditions). For each condition, only the worst case is shown (corners of the planes, which are provided as a guide).**

The ERR is lower by approximately 7% on average with frictionless contact (Figure 11-b), because only sliding at the interface occurs in all cases. The ERR after the first thermal cycle is lower for the interface  $a_1$  (upper) than for  $a_2$  (lower) by about 10% and 5%, respectively with FBC and PBC, i.e. opposite to the ERR calculated without frictionless contact. Frictionless contact does not change the overall trends after the second thermal cycle: all counter-flow cases are more critical than co-flow with  $PR=0.5$ . For all polarization cases, the ERR calculated with frictionless contact is also always higher at the outlet than at the inlet manifold sealant. For all counter-flow cases ( $PRF$  degree=0.1, 0.5 and 1.0), the ERR calculated with frictionless contact is higher than after the first thermal cycle. Similarly to the ERR calculated without frictionless contact, the most critical case is CR 0.5, where the ERR increases by about 10%. After the second thermal cycle with 0.7 mm thick sealant, the interface  $a_2$  (lower) is more critical than  $a_1$  (upper).

Figure 12 provides an overview of the worst case for each operation point and model assumption, for comparing the ERR computed for sealant thicknesses of 0.2 mm and 0.7 mm. The difference between the boundary conditions FBC and PBC is also large and follows the same trend regardless of the thickness of the sealant. The reduction of the sealant thickness to 0.2 mm is beneficial and yields a decrease of the ERR by about 25 %. This trend is approximately the same for both the first and second thermal cycles.



### Summary of Sealing Failure:

From the results, the risk of sealants failure:

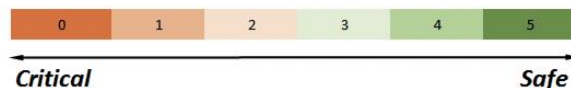
- is reduced for thinner sealants. The thinner sealants were found beneficial also for the contact pressure. However, modelling artefacts also contributed to this last improvement;
- is reduced at the two MIC units near the end plates. In terms of design, this means that large stacks made by sub-assemblies with intermediate separation are favoured;
- is the lowest for operation in co-flow;
- decreases after long-term polarisation in co-flow combined with thermal cycling, whereas it increases if the polarization is in counter-flow. The worst condition is counter-flow with prereforming degree of 0.5.

## 2.6 Summary of thermo-mechanical durability modelling

The table below provides a qualitative summary of the severity of the thermo-mechanical issues as a function of the CH2P stack operating modes and design, in a color-coded manner from dark orange (detrimental/critical) to green (beneficial/safe) for comparative purposes. (BC: boundary conditions, PBC: modified periodic boundary conditions, FBC: flat boundary conditions, MIC: interconnect, CO: co-flow, CR: counter-flow. “2Def00”, “1DefA/B”, “2DefA/B” correspond to MIC pre-deformation profiles).

**Table 2: Summary of thermo-mechanical issues severity as a function of the operating mode**

Model	BC	MIC	Operation	Sealant thickness (mm)	Contact Pressure			Cell failure			Sealants failure		
					Qualification	Operation	Thermal cycling	Qualification	Operation		Thermal cycling	1st Thermal cycle	2nd Thermal cycle
									short-term	long-term			
v1		Ideal	CO 0.5	0.7	4	2	0	NA				1	1
	2Def00			1	1	1	2					2	
v2	PBC	Ideal	CO 0.5	0.2	5	3	3						
				0.7	4	2	2	2	3	4	3	2	2
			5			0	0		5	1			
			4			1	2		4	0			
			3			2	3		4	1			
	1DefA/B	CO 0.5	4	2	2	2	3	4	2	2			
			3	2	2	2	3	4	2	2			
	FBC	CO 0.5	0.2	5	3	3	NA				4	5	
			0.7	4	2	2	1	3	4	3	3	4	
				2	1	1	1	3	4	3	3	4	



### 3 Degradation of the Ni-YSZ electrode microstructure.

This section presents the second degradation phenomenon that mainly affects the SOLIDpower stack operated under CH2P modulating modes, namely microstructural alterations. A special attention has been given to the Ni-YSZ electrode as its degradation represents a bottleneck for SOC industrial deployment [3]. Indeed, the Ni microstructural evolution is the most visible alteration of the H<sub>2</sub> electrode, due to the high Ni mobility and low wettability to the YSZ surface, which relates to interfacial surface tensions at material interfaces.

The microstructural evolutions are meticulously examined in a first place, then the driving forces are discussed in a second one in order to establish the link between the CH2P electrode degradation to its operating mode.

#### 3.1 Microstructural evolution analysis via 3D imaging and characterization

Table 3 lists eight volumes imaged by FIB-SEM serial sectioning and used for the evolution analysis of microstructural changes in the SOLIDpower Ni-YSZ electrode material. The exhaustive description of the sample test conditions as well as of the image processing methods for reconstruction are available in D2.1. A short summary is provided hereafter. Pristine Volume A is selected as Volume 1. Volume 2 was operated for 1.9 kh in a segmented-cell kept at OCV for most of the time. Volume 3 was polarized in SOEC mode for 2 kh. Volumes 4 and 5 belong to the same stack operated for 4.7 kh in SOFC and they were extracted from the gas inlet and outlet regions of the cell, respectively. Volume 6 was tested in SOEC mode for 10.7 kh. Volumes 7 and 8 are from a segmented cell operated for 15 kh in SOFC mode. The former comes from a segment located in the inlet region, while the latter comes from the middle and close to the external border in contact with the sealing. The reconstructed Volumes are from regions next to the interface with the electrolyte.

**Table 3: List of volumes used in this study.**

Volume number	Denomination	Dimensions [ $\mu\text{m}$ ]	Voxel size [nm]
1	Pristine A	17.1-10.0-18.5	7
2	SOFC 1.9 kh – Seg.6	16.7-10.7-16.7	7
3	SOEC 2 kh	17.0-11.5-15.0	10
4	SOFC 4.7 kh - Inlet	21.0-12.0-19.5	10
5	SOFC 4.7 kh - Outlet	9.1-18.2-7.4	7
6	SOEC 10.7 kh	9.7-9.7-9.7	10
7	SOFC 15kh – Seg. 12	17.0-10.7-14.6	10
8	SOFC 15kh – Seg. 19	14.0-11.0-14.0	10

All the relevant microstructural parameters have then been computed on these volumes by using in-house tools described in D2.1.

**Table 4: Metric and topological properties measured on the pristine and aged Ni-YSZ volumes.**

Parameter description	Phase	Volume number								Average standard deviation
		1	2	3	4	5	6	7	8	
Volume fraction [ $\mu\text{m}^3/\mu\text{m}^3$ ]	Pore	0.28	27.88	0.28	0.29	0.31	0.27	0.30	0.30	(0.01)
	YSZ	0.44	44.08	0.44	0.44	0.42	0.43	0.43	0.43	
	Ni	0.28	28.04	0.28	0.27	0.27	0.29	0.27	0.27	
$d_{50,s}^1$ [ $\mu\text{m}$ ]	Pore	0.72	0.67	0.76	0.75	0.85	0.76	0.85	0.72	(0.02)
	YSZ	0.84	0.89	0.88	0.87	0.84	0.87	0.88	0.85	
	Ni	0.88	0.96	1.04	1.03	1.08	1.09	1.06	1.05	
$d_{50,r}^2$ [ $\mu\text{m}$ ]	Pore	0.40	0.37	0.41	0.39	0.43	0.42	0.43	0.39	(0.02)
	YSZ	0.38	0.40	0.42	0.40	0.41	0.39	0.39	0.39	
	Ni	0.46	0.55	0.62	0.64	0.63	0.65	0.63	0.63	
Density of TPBs [ $\mu\text{m}/\mu\text{m}^3$ ]	Total	8.7	8.0	6.4	6.4	5.6	6.0	5.4	6.9	(0.23)
	Connected	7.2	6.2	4.8	4.9	4.5	4.7	4.5	5.5	
Interfacial Surface Area <sup>3</sup> [ $\mu\text{m}^2/\mu\text{m}^3$ ]	YSZ/Pore	1.57	1.50	1.55	1.66	1.53	1.54	1.56	1.71	(0.03)
	Ni/Pore	0.56	0.50	0.38	0.41	0.34	0.36	0.32	0.38	
	Ni/YSZ	1.16	1.13	0.98	0.92	0.96	1.01	0.96	0.90	
Total Surface Area [ $\mu\text{m}^2/\mu\text{m}^3$ ]	Pore	2.14	2.00	1.93	2.06	1.87	1.90	1.88	2.09	(0.04)
	YSZ	2.74	2.63	2.53	2.58	2.49	2.55	2.52	2.60	
	Ni	1.72	1.63	1.36	1.33	1.29	1.37	1.28	1.28	
Contiguity [ $\mu\text{m}^3/\mu\text{m}^3$ ]	Pore	0.97	0.96	0.99	0.99	0.99	0.99	0.99	0.98	(0.01)
	YSZ	1.00	1.00	1.00	1.00	1.00	1.00	1.00	1.00	
	Ni	0.97	0.96	0.93	0.90	0.94	0.92	0.95	0.96	
Surface to Volume ratio $S_v$ [ $\mu\text{m}^{-1}$ ]	Pore	7.6	7.9	6.9	7.1	6.1	6.9	6.4	7.1	(0.1)
	YSZ	6.2	5.8	5.8	5.9	5.9	5.9	5.8	6.0	
	Ni	6.2	5.5	4.8	4.9	4.7	4.7	4.8	4.7	

<sup>1</sup>Median phase diameter measured by overlapping spheres.

<sup>2</sup>Median phase diameter measured by ray tracing.

<sup>3</sup>Interfacial Surface Area values SA values were adjusted by multiplying with the factor  $\pi/6$  to estimate the actual surface area from the digitized Volume assuming close to spherical shapes.

The coarsening of the Ni phase is as expected clearly indicated by the increase of the Ni median diameter  $d_{50}$  (approximately 33% after 2 kh in SOEC and 4.7 kh in SOFC operation). The measurements also suggest a slight increase of the YSZ median diameter with respect to the pristine volume, which however cannot be ascertained statistically with the present dataset. Volumes 2 and 3 exhibit a significant difference in Ni  $d_{50}$ , despite a similar testing time of 1.9 kh and 2 kh, respectively. Therefore, the difference may be due to polarization and or gas composition effects, since Volume 2 was polarized in SOEC, whereas Volume 3 was at OCV under SOFC gas and temperature conditions for most of the time.

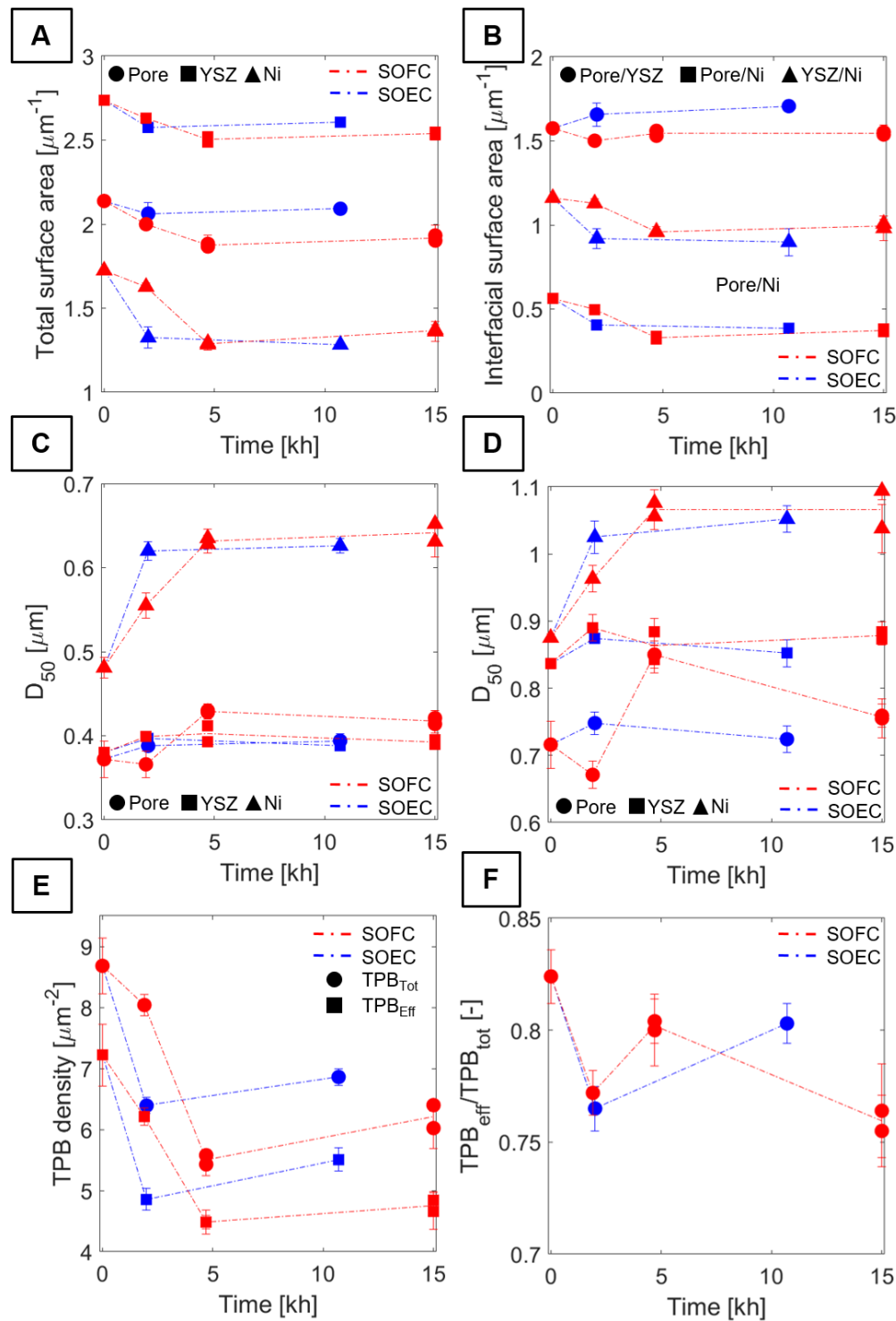
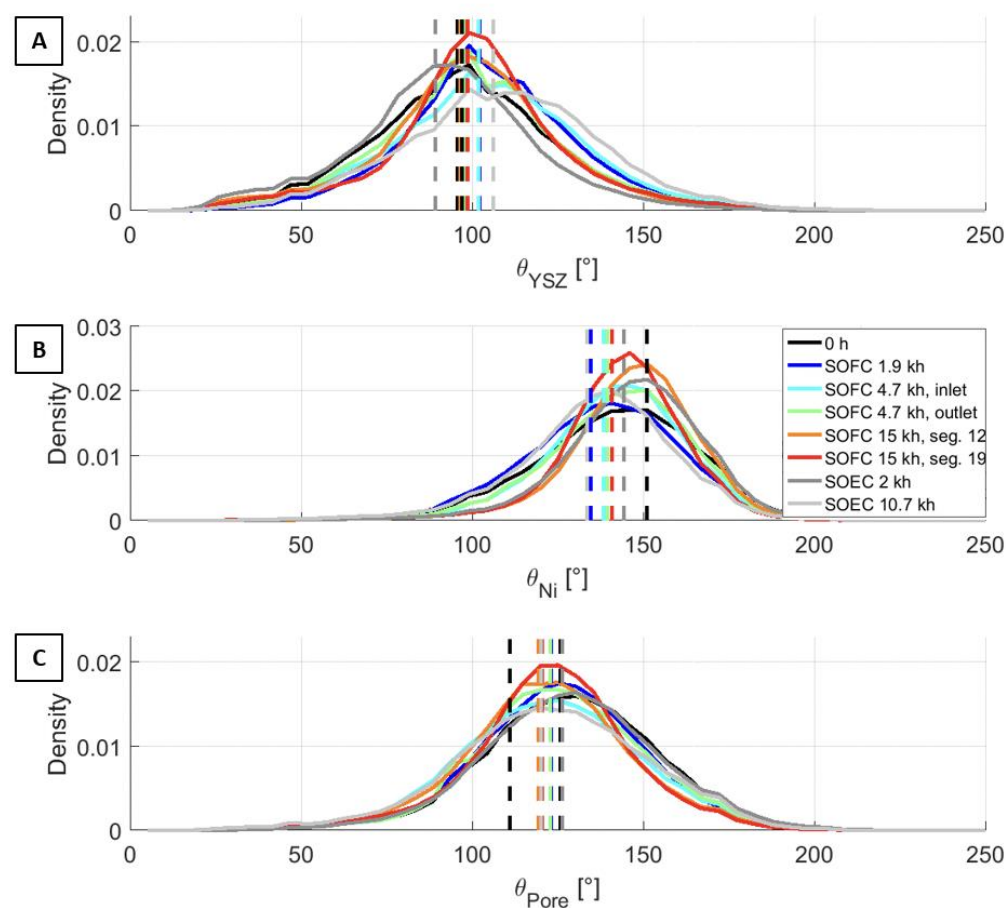


Figure 13: Evolution of measured topological properties (data referred to Table 5.1): (A) total surface areas, (B) interfacial surface areas, (C, D): median phase diameter measured by overlapping spheres (C) and ray tracing (D), density of total and connected TPB (E) and their ratio (F). Measurements on Volumes aged under SOFC and SOEC are shown in red and blue, respectively. The trend lines and error bars are provided as a guide for the eye; the latter were estimated based on measurement of sub-volumes with a size of  $9^3 - 10^3 \mu\text{m}$ .

The increase in  $d_{50}$  and decrease in Ni total surface area cause as expected a diminution of the total and connected TPB density. Significant changes in phase volume fraction are not observed. A stabilization is afterwards observed, except for the Ni contiguity upon SOFC operation, which also leads to a further decrease in the ratio  $TPB_{eff}/TPB_{tot}$  (Figure 14). The results are in line with the stability of the contributions of Ni charge-transfer and gas-phase transport to the total ASR measured by EIS in SOFC mode. Further, the accessible TPB analysis available until 4.7 kh [17] suggests that a large degradation of the transport properties does not occur during this time span. The standard metrics do however not provide sufficient sensitivity to determine whether or not a stable state has been reached. The Ni median diameter measured by filling by overlapping monosized spheres is close to the limits predicted by the 2D or 3D version of the Zener equation for incoherent or coherent interfaces, respectively. The agreement suggests that the constrained growth has reached a nearly stable state, but the uncertainty on the applicability limits showcased by the large differences between predictions from the 2D and 3D versions and geometrical assumptions remain too large for assessing the stability in the long-term. Further, significant differences with the expected size distributions are observed, showcasing the difficulties to analyze the long-term microstructural evolution of Ni-YSZ using governing equations for systems dominated by spherical shapes. The measurements also suggest a subtle evolution of the YSZ phase.

The measurement of available length, dihedral angles and interfacial curvature indicate that the microstructure continues to evolve after 2 kh (SOEC) and 4.7 kh (SOFC). It further suggests the presence of two stages in particular in SOFC mode. The distribution of available length associated to each TPB displays a reduction of the spread in the Ni case. That is, a progressive decrease of the shorter and larger lengths and a concurrent accumulation towards the peak values ( $\mu\text{m}$ ) are observed, even though the ISA Pore/Ni initially decrease (up to 4.7 kh) followed by apparent stabilization. The modification of the Pore/YSZ interface is mainly the consequence of the movement of the metallic phase. The measured available lengths on YSZ shift with operation time towards larger values, even if the total ISA Pore/YSZ does not significantly evolve. The detrimental effect on the performance of the measured changes in the available length on Ni and YSZ is likely low.

From the analyzed data, concepts from topological coarsening theory may better describe the observed microstructural changes, with a first stage characterized by the breakdown of the connectivity of the Ni phase, driven by the tendency towards average null mean curvature of the interfacial surfaces and concurrently resulting in a decrease in TPB density. Once this condition is reached, large changes in particles location does not proceed further, while the relocation continues toward the diminution of the larger absolute value of curvatures. Under these assumptions of mild adjustments of interface positions, the TPB density may not further diminish strongly, even though a stable state has not been reached yet. Nevertheless, the rearrangement of the dihedral angles' distributions (Figure 14) does not exclude a further shift of TPB position with the consequent decrease of TPB density.



**Figure 14: Evolution of the YSZ (A), Ni (B) and pore (C) dihedral angle distributions upon operation. The vertical dashed colour lines are the mean of the distributions, while the black ones are the values measured by Nelson et al. [18], respectively 97°, 151° and 111°.**

The YSZ phase is central for the stability of the cermet, which acts as a matrix constraining the relocation of the more mobile Ni phase. The Zener equation informs that higher volume fraction and fine microstructure are desirable. Whenever the constraining function would be altered by e.g. repeated temperature excursions upon transients during load following, Ni relocation would be triggered with the risk of a consequent decrease of electrochemical active sites. The analysis in the view of pinning and the lowest YSZ dihedral angles however suggests that a significant share of the morphological features allowing an efficient constraint of the Ni phase are fine and henceforth potentially affected first by YSZ coarsening. Another practical related open question is whether the close to equilibrated state is dependent only upon the YSZ microstructure, which would allow the screening of a-priori redox-tolerant microstructures.

## 3.2 Driving forces that affect the stability of the electrode microstructure

### 3.2.1 Effect of overpotential

We examined the possibility that the applied polarization influences interfacial surface tensions in the Ni-YSZ electrode. The electrowetting phenomenon is investigated as a candidate mechanism for the observed difference between SOFC and SOEC operation. The theory predicts a modification in wettability (hence of the dihedral angles) upon the application of a difference

in electrostatic potential between an electrode and electrolyte (usually liquid). This phenomenon is commonly studied by measuring variations in dihedral angles at the interfaces formed by liquid drops on flat solid surfaces [19–21].

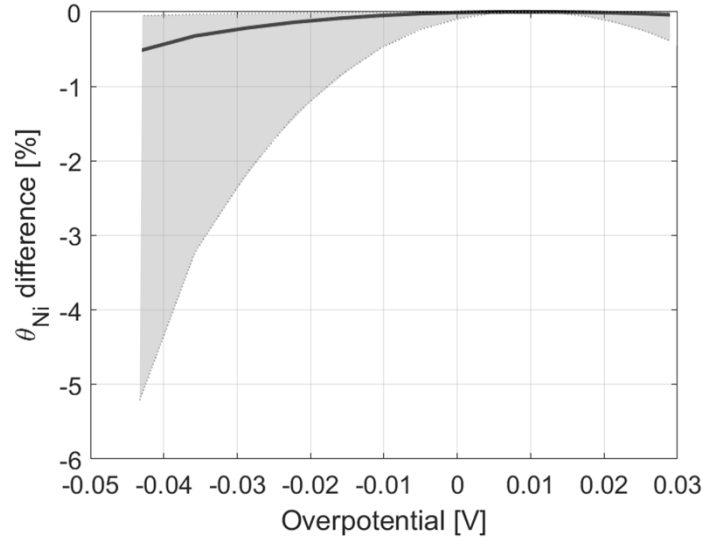


**Figure 15: Computed variation of  $\theta_{Ni}$  under polarization. The maximum value corresponds to  $140^\circ$ . Negative values comport a decrease of the angle, therefore higher wettability. The shaded area displays the variation of  $\pm 1$  order of magnitude of the Ni/YSZ interfacial capacitance values.**

The electrowetting theory describes the dependence of the interfacial surface energy on the applied electrical field across the interface and was established for solid-liquid electrolyte systems. In the case of relevance for polarized Ni/YSZ interfaces, a change in Ni dihedral angle  $\theta_{Ni}$  is first anticipated. Indeed, the higher Ni mobility may result in morphological changes resembling those measurable for liquid systems. The relationship between the Ni dihedral angle and the variation in applied potential ( $\epsilon$ ) is as follows:

$$\sin(\theta_{Ni}(\epsilon)) = \gamma_{YSZ/Pore} \sin \theta_{Pore} \left( \gamma_{YSZ/Pore} \frac{\sin \theta_{Pore_0}}{\sin \theta_{Ni_0}} - \frac{C_D}{2} (\epsilon - \epsilon_0)^2 \right)^{-1} \quad (3)$$

$\theta_{Pore_0}$  and  $\theta_{Ni_0}$  refer to the dihedral angles at the pzc (point of zero charge).

### 3.2.2 Effect of oxygen partial pressure

Jiao et al. [22] investigated the evolution under polarization of a patterned Ni-film anode sputtered on a YSZ substrate, detecting a strong relocation of Ni due to the increase in wettability. The difference in partial pressure of the oxygen adsorbed on the Ni surface near the TPB, due to the generation and consumption of surface species was discussed as a tentative explanation. The increase of oxygen activity on the adsorption sites would lead to the reduction of surface tension (and reduction of the Ni dihedral angle). The oxygen activity is related to the  $H_2O$  partial pressure in the gas phase near the TPB, which differs from the bulk value according to the applied current density. The above-mentioned relationships described in [22] are displayed in Figure 16. Variations of  $p_{H_2O}$  below 0.8 atm would not strongly modify the Ni angle, while a greater humidity would cause a surge of wettability.



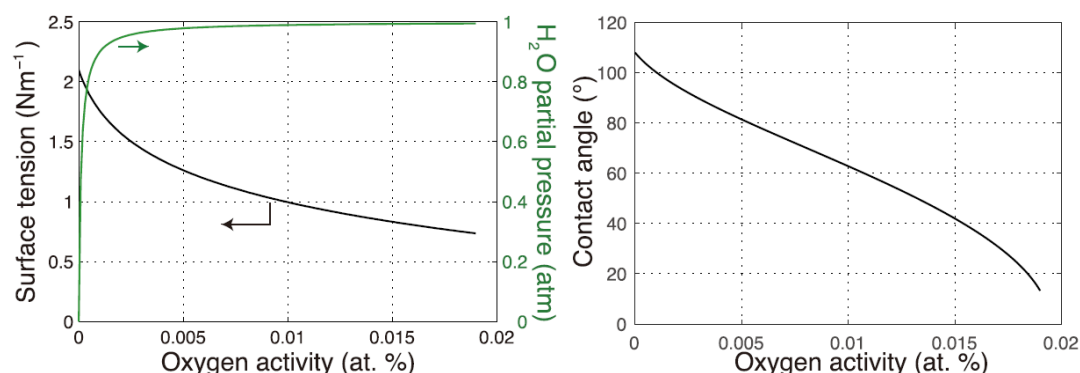


**Figure 16: (left) Dependence of  $a_{O_2}$  ( $Ni$ ) with  $Ni$  surface tension and  $p_{H_2O}$  (gas). (right) Dependence of  $Ni$  dihedral angle with  $a_{O_2}$  ( $Ni$ ) at 800°C. Images obtained from [22].**

Figure 16 shows that the diminution of surface tension and angle becomes significant for steam partial pressures higher than 0.8 atm, which can be met only near the cell inlet in SOEC mode or at the outlet in SOFC mode, under a practical fuel utilization of 80%. A series of clear practical consequences are expected from a direct dependence between wettability and steam partial pressure as shown in Figure 16.

Saiz et al. [23] investigated the dependence of the interfacial tension in metal/oxide systems (i.e. pure metal/ $Al_2O_3$ ) on the partial pressure of oxygen. The work of adhesion (defined as the work needed to reversibly separate the interface) is related to the oxygen activities, following non-linear dependency. Under high  $p_{O_2}$ , the surface tension and in particular the dihedral angle diminishes likewise with oxygen activity, causing an overall augmentation of the work of adhesion. In case of intermediate  $p_{O_2}$ , interfacial tension depends on the oxygen activity and the work of adhesion is similar to the nominal value for pure surfaces. Lastly, under lower  $p_{O_2}$ , a direct dependence between dihedral angle and oxygen activity is observed, but the effect on the adhesion work could not be quantified, due to experimental limitations. In the light of the study by Saiz et al., the effects of oxygen partial pressure could lead to the alteration of the interface and in particular of the dihedral angles under electrolysis condition.

### 3.3 Summary for microstructural evolution modelling

From this study, a straightforward recommendation to mitigate degradation is:

- To operate the CH2P stack at low overpotentials. It can be achieved by an increase of temperature to facilitate charge transfer, which would however also increase the surface diffusion coefficient of Ni. A dependence upon overpotential, i.e. position in the cell is expected.
- Possibilities for mitigation may also be achieved qualitatively by a finer YSZ microstructure next to the electrolyte to limit competitive growth. A finer YSZ electrolyte side may also provide additional sites for pinning the Ni/Pore interface.
- A complementary approach is the modification of the dependence between dihedral angle and overpotential, which may be achieved by targeted doping.

## 4 Conclusions

A multi-scale and multi-physics modelling approach has been proposed in this work to better understand and evaluate the risks of failure that a SOLIDpower stack can face during operation under constant conditions and the modulating CH2P modes. For this purpose, the major degradation phenomena identified in WT2.1, namely thermo-mechanical and microstructural alterations, were examined. On the SRU scale, a 3D FEM model has been employed, and the risk of failure has been examined for every component (cell, sealings, and MICs) while taking into account the complex interactions between them. A special attention has been paid to evaluate the components robustness as a function of the CH2P operating conditions in order to provide insights and recommendations for an optimal operation under CH2P modes. This target has been reached by performing a thorough sensitivity analysis over the operating conditions (pre-reforming degree, load, temperature, sealant thickness, flow direction) as a function of time. Similarly, on the microstructural scale, advanced imaging and characterization techniques have been employed to better understand the alterations that may shorten the cells lifespan. A summary for each stack component failure risk has been given and highlighted. In short, the main guidelines from this work are the following:

- No critical points are anticipated with cells / stacks operated in CH2P mode, i.e. under load cycling between full, partial and OCV ( $H_2$  production through steam reforming).
- The CH2P stack is robust and tolerant enough: good performance and good durability.
- New developed control tool Real Time Optimization (RTO) validated on a SOLIDpower commercial system (BlueGen) proves very promising in ensuring smooth and safe transitions between the operating modes.
- The most critical point remains the start-up phase, and full thermal cycles (seal leakage risk, contact pressure loss).

## Acknowledgment

This project has received funding from the Fuel Cells and Hydrogen 2 Joint Undertaking under grant agreement No 735692. This Joint Undertaking receives support from the European Union's Horizon 2020 research and innovation programme, Hydrogen Europe and Hydrogen Europe Research.

## References

- [1] F. Greco, A. Nakajo, Z. Wullemmin, J. Van herle, The Effects of Component Tolerances on the Thermo-Mechanical Reliability of SOFC Stacks, *ECS Trans.* 78 (2017) 2271–2283. <https://doi.org/10.1149/07801.2271ecst>.
- [2] T. Dey, D. Singdeo, M. Bose, R.N. Basu, P.C. Ghosh, Study of contact resistance at the electrode–interconnect interfaces in planar type Solid Oxide Fuel Cells, *J. Power Sources.* 233 (2013) 290–298. <https://doi.org/10.1016/J.JPOWSOUR.2013.01.111>.
- [3] M. Hubert, J. Laurencin, P. Cloetens, B. Morel, D. Montinaro, F. Lefebvre-Joud, Impact of Nickel agglomeration on Solid Oxide Cell operated in fuel cell and electrolysis modes, *J. Power Sources.* 397 (2018) 240–251. <https://doi.org/10.1016/J.JPOWSOUR.2018.06.097>.
- [4] A. Nakajo, F. Mueller, J. Brouwer, J. Van herle, D. Favrat, Progressive activation of degradation processes in solid oxide fuel cells stacks: Part I: Lifetime extension by optimisation of the operating conditions, *J. Power Sources.* 216 (2012) 449–463. <https://doi.org/10.1016/J.JPOWSOUR.2012.05.078>.
- [5] A. Nakajo, Z. Wullemmin, P. Metzger, S. Diethelm, G. Schiller, J. Van herle, D. Favrat, Electrochemical Model of Solid Oxide Fuel Cell for Simulation at the Stack Scale I. Calibration Procedure on Experimental Data, *J. Electrochem. Soc.* 158 (2011) B1083. <https://doi.org/10.1149/1.3596433>.
- [6] A. Nakajo, P. Tanasini, S. Diethelm, J. Van herle, D. Favrat, Electrochemical Model of Solid Oxide Fuel Cell for Simulation at the Stack Scale II: Implementation of Degradation Processes, *J. Electrochem. Soc.* 158 (2011) B1102. <https://doi.org/10.1149/1.3596435>.
- [7] A. Nakajo, F. Mueller, J. Brouwer, J. Van herle, D. Favrat, Progressive activation of degradation processes in solid oxide fuel cell stacks: Part II: Spatial distribution of the degradation, *J. Power Sources.* 216 (2012) 434–448. <https://doi.org/10.1016/J.JPOWSOUR.2012.05.077>.
- [8] D. Systèmes, Volume IV: Elements, ABAQUS 6.14 Anal. User's Guid. IV (2014).
- [9] F. Greco, Improved thermo-mechanical reliability of anode-supported solid oxide fuel cells PAR, 8470 (2018).
- [10] A. Nakajo, F. Mueller, J. Brouwer, J. Van herle, D. Favrat, Mechanical reliability and durability of SOFC stacks. Part I : Modelling of the effect of operating conditions and design alternatives on the reliability, *Int. J. Hydrogen Energy.* 37 (2012) 9249–9268. <https://doi.org/10.1016/J.IJHYDENE.2012.03.043>.
- [11] A. Nakajo, F. Mueller, J. Brouwer, J. Van herle, D. Favrat, Mechanical reliability and durability of SOFC stacks. Part II: Modelling of mechanical failures during ageing and cycling, *Int. J. Hydrogen Energy.* 37 (2012) 9269–9286. <https://doi.org/10.1016/J.IJHYDENE.2012.03.023>.
- [12] A. Nakajo, Z. Wullemmin, J. Van herle, D. Favrat, Simulation of thermal stresses in anode-supported solid oxide fuel cell stacks. Part I: Probability of failure of the cells, *J. Power Sources.* 193 (2009) 203–215. <https://doi.org/10.1016/J.JPOWSOUR.2008.12.050>.
- [13] A. Nakajo, J. Van Herle, D. Favrat, Sensitivity of stresses and failure mechanisms in SOFCs to the mechanical properties and geometry of the constitutive layers, *Fuel Cells.* 11 (2011) 537–552. <https://doi.org/10.1002/fuce.201000108>.

- [14] M. Hauth, V. Lawlor, P. Cartellieri, C. Zechmeister, S. Wolff, C. Bucher, J. Malzbender, J. Wei, A. Weber, G. Tsotridis, H.L. Frandsen, K. Kwok, T.T. Molla, Z. Wuillemin, J. Van herle, F. Greco, T. Cornu, A. Nakajo, A. Atkinson, L. Vandeperre, X. Wang, Production and Reliability Oriented SOFC Cell and Stack Design, *ECS Trans.* 78 (2017) 2231–2249. <https://doi.org/10.1149/07801.2231ecst>.
- [15] A. Müller, S. Goswami, W. Becker, D. Stolten, L.G.J. De Haart, R.W. Steinbrech, Assessment of the sealing joints within SOFC stacks by numerical simulation, *Fuel Cells.* 6 (2006) 107–112. <https://doi.org/10.1002/fuce.200500115>.
- [16] D. Gross, Thomas Seelig, *Fracture Mechanics With an Introduction to Micromechanics*, 2011. <https://doi.org/10.1002/9781118097298.weoc096>.
- [17] A. Nakajo, A.P. Cocco, M.B. DeGostin, P. Burdet, A.A. Peracchio, B.N. Cassenti, M. Cantoni, J. Van herle, W.K.S. Chiu, Evolution of 3-D Transport Pathways and Triple-Phase Boundaries in the Ni-YSZ Hydrogen Electrode upon Fuel Cell or Electrolysis Cell Operation, *ECS Trans.* 78 (2017) 3205–3215. <https://doi.org/10.1149/07801.3205ecst>.
- [18] G.J. Nelson, K.N. Grew, J.R. Izzo, J.J. Lombardo, W.M. Harris, A. Faes, A. Hessler-Wyser, J. Van herle, S. Wang, Y.S. Chu, A. V. Virkar, W.K.S. Chiu, Three-dimensional microstructural changes in the Ni-YSZ solid oxide fuel cell anode during operation, *Acta Mater.* 60 (2012) 3491–3500. <https://doi.org/10.1016/J.ACTAMAT.2012.02.041>.
- [19] A. Quinn, R. Sedev, J. Ralston, Contact angle saturation in electrowetting, *J. Phys. Chem. B.* 109 (2005) 6268–6275. <https://doi.org/10.1021/jp040478f>.
- [20] T.B. Jones, On the relationship of dielectrophoresis and electrowetting, *Langmuir.* 18 (2002) 4437–4443. <https://doi.org/10.1021/la025616b>.
- [21] A. Quinn, R. Sedev, J. Ralston, Influence of the electrical double layer in electrowetting, *J. Phys. Chem. B.* 107 (2003) 1163–1169. <https://doi.org/10.1021/jp0216326>.
- [22] Z. Jiao, N. Shikazono, Study on the effects of polarization on local morphological change of nickel at active three-phase-boundary using patterned nickel-film electrode in solid oxide fuel cell anode, *Acta Mater.* 135 (2017) 124–131. <https://doi.org/10.1016/J.ACTAMAT.2017.05.051>.
- [23] E. Saiz, R.M. Cannon, A.P. Tomsia, High-Temperature Wetting and the Work of Adhesion in Metal/Oxide Systems, *Annu. Rev. Mater. Res.* 38 (2008) 197–226. <https://doi.org/10.1146/annurev.matsci.38.060407.132443>.